Application of improved CFD modeling for prediction and mitigation of traffic-related air pollution hotspots in a realistic urban street

Reference:
Lauriks Tom, Longo Riccardo, Baetens Donja, Derudi Marco, Parente Alessandro, Bellemans Aurélie, van Beeck Jeroen, Denys Siegfried.- Application of improved CFD modeling for prediction and mitigation of traffic-related air pollution hotspots in a realistic urban street
Atmospheric environment : an international journal - ISSN 1352-2310 - 246(2021), 118127
Full text (Publisher's DOI): https://doi.org/10.1016/J.ATMOSENV.2020.118127
To cite this reference: https://hdl.handle.net/10067/1739170151162165141

Application of improved CFD modeling for prediction and mitigation of traffic-related air pollution hotspots in a realistic urban street

Tom Lauriks[a,b], Riccardo Longo[c,d], Donja Baetens[a], Marco Derudi[d], Alessandro Parente[c,e], Aurélie Bellemans[c,e,f], Jeroen van Beeck[b], Siegfried Denys[a]

[a] *University of Antwerp - Research group Sustainable Energy, Air and Water Technology, Groenenborgerlaan 171, 2020 Antwerp, Belgium*
[b] *von Karman Institute for Fluid Dynamics - Environmental and Applied Fluid Dynamics department, Waterloosesteenweg 72, 1640 Sint-Genesius-Rode, Belgium*
[c] *Université libre de Bruxelles - Aéro-Thermo-Mécanique Department*
[d] *Politecnico di Milano - Dipartimento di Chimica, Materiali ed Ingegneria Chimica "G. Natta"*
[e] *Combustion and Robust Optimization Group (BURN), Université libre de Bruxelles and Vrije Universiteit Brussel, Bruxelles, Belgium*
[f] *University of Texas at Austin - Department of Aerospace Engineering and Engineering Mechanics, TX, USA*

Abstract

The correct prediction of air pollutants dispersed in urban areas is of paramount importance to safety, public health and a sustainable environment. Vehicular traffic is one of the main sources of nitrogen oxides (NO_x) and particulate matter (PM), strongly related to human morbidity and mortality. In this study, the pollutant level and distribution in a section of one of the main road arteries of Antwerp (Belgium, Europe) are analyzed. The assessment is performed through computational fluid dynamics (CFD), acknowledged as a powerful tool to predict and study dispersion phenomena in complex atmospheric environments. The two main traffic lanes are modeled as emitting sources and the surrounding area is explicitly depicted. A Reynolds-averaged Navier–Stokes (RANS) approach specific for Atmospheric Boundary Layer (ABL) simulations is employed. After a validation on a wind tunnel urban canyon test case, the dispersion within the canopy of two relevant urban pollutants, nitrogen dioxide (NO_2) and particulate matter with an aerodynamic diameter smaller than 10 µm (PM_{10}), is studied. An experimental field campaign led to the availability of wind velocity and direction data, as well as PM_{10} concentrations in some key locations within the urban canyon. To accurately predict the concentration field, a relevant dispersion parameter, the turbulent

ABL: Atmospheric Boundary Layer, BIA: building influence area, DNS: direct numerical simulations, ESP: electrostatic precipitation, EU: European Union, GCI: grid convergence index, NLEV: Non-Linear Eddy-Viscosity, VMM: Flanders Environment Agency

*Corresponding author's email: tom.lauriks@uantwerpen.be ; riccardo.longo@ulb.ac.be

Schmidt number, Sc_t, is prescribed as a locally variable quantity. The pollutant distributions in the area of interest - exhibiting strong heterogeneity - are finally demonstrated, considering one of the most frequent and concerning wind directions. Possible local remedial measures are conceptualized, investigated and implemented and their outcomes are directly compared. A major goal is, by realistically reproducing the district of interest, to identify the locations inside this intricate urban canyon where the pollutants are stagnating and to analyze which solution acts as best mitigation measure. It is demonstrated that removal by electrostatic precipitation (ESP), an active measure, and by enhancing the dilution process through wind catchers, a passive measure, are effective for local pollutant removal in a realistic urban canyon. It is also demonstrated that the applied ABL methodology resolves some well known problems in ABL dispersion modeling.

Keywords

Atmospheric environment; Air Pollution; Computational Fluid Dynamics (CFD); Mitigation Strategy; Sustainability; Natural Ventilation;

1. Introduction

1.1. Origins and spatial distribution of air pollution

In the last decades, pollutant dispersion within the urban canopy has severely affected public breathability and homeland security, leading to a relevant number of environmental issues (Buccolieri et al., 2010). Considering the unceasing urbanization, the majority of the people in the world is estimated to be living in urban areas (Manning, 2011), further emphasizing this environmental issue.

According to recent reports (Karagulian et al., 2015; Longo et al., 2020a), the main causes to urban air pollution are traffic (25 %), followed by combustion and agriculture (22 %), domestic fuel burning (20 %), natural dust (18 %) and industrial activities (15 %). As stated by Zhong et al. (2016), the urban environment tends to limit the effective ventilation of gaseous pollutants, comporting a further lowering of the outdoor air quality (Pontiggia et al., 2010). Moreover, the stagnant outdoor pollutants can easily access indoor environment through windows and the ventilation system (Chávez Yáñez, 2014). In this scenario, a further alarming prediction comes from the Organization for Economic Cooperation and Development (OECD), according to which, air pollution is expected to become the world's first environmental cause of premature mortality by 2050 (Blocken et al., 2016; OECD, 2012).

Particulate matter (PM), nitrogen dioxide (NO_2), ozone (O_3) and sulfur dioxide (SO_2) are the pollutants with the strongest evidence of health effects (WHO, 2019). In fact, NO and NO_2 are frequently combined into the term NO_x (Logan, 1983) and particulate matter with an aerodynamic diameter smaller than 2.5 and 10 µm ($PM_{2.5}$ and PM_{10} respectively) are relevant subdivisions of PM (WHO, 2018). All these substances - NO, NO_2, $PM_{2.5}$, and PM_{10} - have been associated to adverse health effects (Atkinson et al., 2013; Bazyar et al., 2019; Guarnieri and Balmes, 2014; White et al., 2018). According to the latest numbers of the EEA (2019b), road transport causes 39 % of the European NO_x emissions and 15.8 % and 14.4 % - respectively - of the primary $PM_{2.5}$ and PM_{10} emissions (EEA, 2018). As a consequence, studying traffic emissions in urban environments both for NO_x and PM remains a meaningful task.

In this regard, the WHO (2018) is in charge of an “urban air quality database” - consisting mainly of PM_{10} and $PM_{2.5}$ annual mean data collected in human settlements. This data suggests that, while air pollution concentrations of PM were approximately stable on a global scale in the period 2010-2016, in some areas (i.e. the Americas and Europe) it was decreasing. However, the WHO (2018) states that for solid conclusions on trends in air pollution, more detailed analyses over longer temporal intervals are necessary. Considering NO_x, decreases are also observed in the last decades (EEA, 2019a; OECD, 2019). Nevertheless, sixteen countries of the European Union (EU) still registered NO_2 concentrations exceeding the annual prefixed limit value (EEA, 2019b). In addition, the number of measurement stations upon which the European Environment Agency (EEA) statistics are based is limited (EEA, 2019c). As a consequence, more detailed measurements are needed, both for NO_x and PM.

For example, in Flanders (Belgium), yearly average NO_2 concentrations exceeded the European limit value in 2017 at only one measurement station (VMM, 2018). These considerations are however based on just 51 measurement stations, and the actual situation could be more alarming. Figure 1 (a) demonstrates the scarcity of these measurement stations in the center of Antwerp, in Flanders. Modeling results (e.g. Figure 1 (a) of VMM (2019)) and local measurement campaigns (e.g. Figure 1 (b) of Meysman and De Craemer (2018)) indicate that at many other locations with heavy traffic, the annual average European limit value for NO_2 of 40 µg/m^3 was exceeded (VMM, 2018). This further emphasizes the need to investigate air pollution more in detail on district scales: to analyze how the local urban features can affect the pollutant level, whether very localized pollution hotspots exist, and to evaluate the performance of local remedial measures.

In this study, the main focus was on the evaluation of the pollution level on a very detailed spatial scale in a portion of the Turnhoutsebaan street of Antwerp. Its location is shown in Figures 1 (a) and (b). Figures 1 (a) and (b) also display previously established NO_2 concentrations in the Turnhoutsebaan (Meysman and De Craemer, 2018; VMM, 2019), on a less detailed spatial scale with respect to the one used in this study (the result in Figure 1 (a) was obtained using a model that parametrizes the wind flow at the street level (Aarhus University, 2020; VMM, 2019)). Figure 1 (b) suggests that the Turnhoutsebaan is clearly problematic regarding NO_2 concentration and that a more detailed analysis is necessary. The Turnoutsebaan is characterized by intense traffic, high buildings, and a relatively narrow street width, which could restrict the natural ventilation. These characteristics can be assumed as the cause of the bad air quality and this hypothesis will be investigated in this study. It was also investigated whether very localized pollution hotspots exist, considering the previous evidence of the strong heterogeneity of pollutant distributions within the urban framework (Blocken et al., 2016) delivered by observations and measurement campaigns with a high spatial resolution performed in other cities. For example in a street in downtown Sydney (Australia) on a distances of just 200 m, differences in average $PM_{2.5}$ concentration of approximately 15 µg/m^3 were observed (Wadlow et al., 2019). In a small scale area in Liege (Belgium), measurements indicated that at a distance of 50 m, a difference in mean PM_{10} of more than 20 µg/m^3 occurred (Merbitz et al., 2012). Similar observations were made in Hong Kong (Li et al., 2018b), Oakland (California, USA) (Apte et al., 2017) and the Berlin/Brandenburg Metropolitan Region (Germany) (Bonn et al., 2016).

1.2. Available local mitigation measures

Since strong concentration gradients occur in urban areas, investigating the application of local mitigation measures to reduce pollutant levels at concentration hotspots could substantially contribute to healthier cities. Within the framework of local air pollution mitigation, Vardoulakis et al. (2018) listed a number of possible remedial strategies, consisting mostly of some form of emission reduction. However, the majority of the proposed individual measures resulted in a limited benefit, or involved structural changes such as reducing the need for motorized trips. The latter can be achieved by regulations and interventions that discourage private car usage and investing in alternative transportation means (Quarmby et al., 2019). However, redistributing road space in favor of non-car transportation can be technically challenging and politically sensitive (European Commission, 2004). Hence, these structural changes will not be a fast process and additional measures might be interesting. Possibilities include removal by vegetation, removal by photocatalysis, electrostatic precipitation, and adapting building geometries to enhance natural ventilation and dilution. Besides, even if structural changes would solve most problems, the additional measures could still be interesting for connecting roads, where traffic cannot be reduced.

The controversial effect of vegetation on air pollution has already been extensively studied (e.g. by Abhijith and Gokhale (2015); Buccolieri et al. (2011); Jeanjean et al. (2017), and Salmond et al. (2013)). Vegetation can remove both gaseous (Abhijith et al., 2017) and particulate pollutants (Janhäll, 2015). However, it also affects the velocity field which, in turn, can reduce the dilution process, negatively impacting the concentration level (Vos et al., 2013).

Photocatalysis, which involves the use of light and a solid catalyst, is capable of completely mineralizing many air contaminants (Ollis, 2000), thereby converting them to products that are less harmful for human health and environmentally more acceptable (de Richter and Caillol, 2011). It can decompose constituents of PM (de Richter and Caillol, 2011; Misawa et al., 2020), and remove NO_x from the air (Nguyen et al., 2020). High removal percentages are typically obtained under laboratory conditions, e.g. (Papailias et al., 2015; van Walsem et al., 2018, 2019; Wang et al., 2019). However, realistic atmospheric conditions can greatly reduce photocatalytic degradation, which can be caused by fouling of the photocatalytic surface, and sub-optimal air flow rates and air humidities. A too high relative air humidity can lower the degradation (Mamaghani et al., 2017; Shayegan et al., 2018; Zhang et al., 2020), which can reduce the on-site efficiency (Boonen and Beeldens, 2014). High air speed increases mass transport to the photocatalytic surface, but at the cost of lower pollutant-surface contact times, which ultimately decreases the degradation (Mamaghani et al., 2017; Shayegan et al., 2018; Zhang et al., 2020). This could partly explain why no reduction was observed in a study where photocatalyst was applied in a tunnel for NO_x abatement purposes (Gallus et al., 2015a), since a high wind speed (up to 3 m/s) occurred in the tunnel (Boonen and Beeldens, 2014). In addition, Gallus et al. (2015a) identified deactivation of the photocatalyst in the heavily polluted tunnel conditions due to the adsorption of particles onto the photocatalytic surface, as part of the explanation of the failure of the tunnel experiment. Moreover, in an experimental scale artificial street canyon, an upper limit of 2 % NO_x removal was observed (Gallus et al., 2015b), attributed to limitations of transport of the pollutants to the photocatalytic surfaces. Gallus et al. (2015b) analyzed former similar researches (e.g. the studies of Ballari and Brouwers (2013); Guerrini and Peccati (2007) and Maggos et al. (2008)) and estimated that in realistic urban conditions a daily averaged (24 h cyclus) reduction of NO_x of around 2 % should be obtained. Besides, applying photocatalysis to purify air pollutants can result in the formation of harmful by-products (Gallus et al., 2015b; Mamaghani et al., 2017; Shayegan et al., 2018). This should certainly be investigated more thoroughly before implementing large scale photocatalytic air purification in public spaces.

As for the local urban geometry/configuration, its significant role in influencing the wind flow (Chew and Norford, 2019; Ricciardelli and Polimeno, 2006) and the pollutant concentration at lower heights (Hang et al., 2012; Kastner-Klein et al., 1997; Wedding et al., 1977) has already been demonstrated. For idealized high-rise compact urban areas, it was demonstrated that varying the height of the buildings and the ratio of built-to-open-space (making one section of the building permeable to air e.g.) can affect the wind speed in the urban canopy (Hang and Li, 2010). Since the increase of wind speed is normally associated with a higher dilution process (Huang et al., 2000), a targeted design and modification of the urban geometry can be acknowledged as an interesting air pollution mitigation measure. A number of potentially beneficial building geometry adaptions have already been suggested by Voordeckers et al. (in press), including the reduction of street canyon length and the increase of street canyon permeability. Shen et al. (2017) noted that, despite the fact that the relation between the urban configuration/geometry and air quality was already extensively studied, only few studies investigated realistic geometries. Mostly simplistic configurations were studied, such as two-dimensional (2D) case studies, e.g. by Aliabadi et al. (2017); Mei et al. (2018); Zhang et al. (2019), or idealized three-dimensional (3D) geometries, e.g. by Hang et al. (2012); Hao et al. (2019); Kastner-Klein et al. (1997); Lin et al. (2019); Tan et al. (2019); Wedding et al. (1977). In the studies of Ghassoun and Löwner (2017); Löwner and Ghassoun (2018); Shi et al. (2018), pollution levels were correlated to urban geometric characteristics - such as average building height, standard deviation of building height, and ratio built to total area - through statistical modeling. Other authors, Gousseau et al. (2011); Panagiotou et al. (2013); Shalaby et al. (2018); Shen et al. (2017); Tominaga (2012); Xie and Castro (2009), focused on the influence of urban geometric features (orientation of the street network relative to the prevailing wind and amount of open space between buildings in a street canyon) on wind flow patterns and/or pollution. In this regard, only few studies modeled the implementation of the aforementioned remediation measures in realistic urban cases (Fu et al., 2017; Juan et al., 2017; Niu et al., 2018). Moreover, these measures were mostly suitable for incorporation into future planning, like creating a large opening in a tall building (An et al., 2019), or different shapes and orientations of entire building blocks (Kurppa et al., 2018). As a consequence, the application of realistically attainable geometric changes to an existing urban case has not yet been thoroughly investigated.

Finally, electrostatic precipitation (ESP) is a technology that efficiently removes small particles from a carrier gas (Calvert, 1990). Blocken et al. (2016) modeled the removal of PM from semi-enclosed parking garages through ESP and the consequent effect on the surrounding urban neighborhood. The results indicated that PM concentrations could be lowered 10-50 % in the vicinity of the parking garages. Vervoort et al. (2019) modeled the removal of $PM_{2.5}$ with ESP from the naturally ventilated courtyard of the American embassy school in Delhi. Up to 34.1% overall volume-averaged concentration reduction was obtained as model result. This technology is promising and interesting, especially in case emission reduction by other means is not possible.

In conclusion, concerning local air pollution mitigation, emission reduction is already known as measure that can mostly be applied, but its effects are either marginal or hard to be quickly achieved. As a consequence, additional measures are necessary to resolve urgent air pollution problems in urban context. Removal by vegetation and photocatalysis are possible local mitigation measures, but the first was already extensively studied and the application of the latter in realistic atmospheric conditions can still be problematic (e.g. low removal percentages and formation of harmful by-products). Intelligently designing and modifying the local urban geometry to dilute air pollution was also identified as an interesting measure. However, research on the attainable application of this measure in existing and realistic urban settings is still lacking. In addition, pollutant removal by ESP was already shown to attain high removal efficiency in ambient air, but its effect in an urban street canyon was not yet investigated. For these reasons, the two latter measures were investigated in this research.

1.3. Research summary and goals

Computational fluid dynamics (CFD), acknowledged as an important instrument to study turbulence and dispersion fields in an atmospheric context (Longo et al., 2019; Piroozmand et al., 2020), is employed in this study. To improve the representation of the flow field with respect to the standard models, a Reynolds-averaged Navier–Stokes (RANS) approach specific for Atmospheric Boundary Layer (ABL) simulation (Longo et al., 2017, 2020b; Longo, 2020) is applied. Moreover, to reliably predict the concentration pattern, a variable turbulent Schmidt number, Sc_t, is implemented, based on the work by Longo et al. (2020a). The model is initially validated over a scaled wind tunnel test case provided with experimental data. The subsequent step is the real scale simulation of pollutant dispersion in an area enveloping a part of the Turnhoutsebaan. The latter is reliably reproduced, explicitly depicting the surrounding roughness elements. One wind direction, among the most frequent and badly affecting the pollutant dispersion, is considered. A field measurement campaign led to the availability of velocity and concentration data in some key locations within the street canyon, further validating the adopted computational methodology. A clear indication of the pollutant distributions inside the area of interest is finally achieved. On the basis of the concentration patterns, three additional configurations meant to reduce localized elevated pollutant levels of the Turnhoutsebaan area are conceptualized and studied. The first one consists in a number of wind catchers located on the roof of selected buildings facing the main street. The second one is based on a feasible building geometry modification, namely the recursive substitution of the pitched roofs with flat ones at a specific location of the Turnhoutsebaan. Both strategies can be considered as passive measures for reducing the pollution level, acting on the local flow field nature and, consequently, on the related dilution process. Finally, an active remedial measure is analyzed, namely the employment of ESP devices in or close to the pollutant stagnation areas detected through CFD within the Turnhoutsebaan. Conclusion are drawn in the last section, together with considerations on the achieved results and the perspective for future work.

The aim of this study is somewhat multifaceted, but the main targets are:

1. to search for relevant traffic-related air pollutant concentration patterns on detailed spatial scales in an urban street, by CFD modeling of NO_2 and PM_{10} traffic emissions;
2. to test and analyze the behavior of an advanced ABL turbulence and dispersion model in a realistic and complex urban street;
3. to conceptualize and employ different realistic and feasible mitigation measures that can be applied locally at pollution hotspots;
4. to detect which of the proposed strategies act as the most performing remediation measure.

2. Methodology

The accurate prediction of pollutant dispersion in urban areas is far from being straightforward (Parente et al., 2017, 2019). This is mainly related to the complex nature of atmospheric flows and to the presence of intricate district configurations and roughness elements (Shen et al., 2015; Yu and Thé, 2016). Urban orography, consisting of varied geometries, shapes and heights, drastically affects the mean flow and its turbulence characteristics. This, in turn, strongly influences the pollutant dispersion and distribution (Hang et al., 2012; Yu and Thé, 2016).

CFD is nowadays considered as a powerful instrument to predict dispersion patterns (Busini and Rota, 2014; Longo et al., 2019; Parente et al., 2017). Differently from Gaussian and Integral models, it can account for varied meteorological conditions, detailed characterization of the pollutant sources, chemical reactions and presence of complex obstacles (Derudi et al., 2014). Nevertheless, commercial CFD codes do not provide specific turbulence models for ABL simulation (Pontiggia et al., 2010). As a matter of fact,

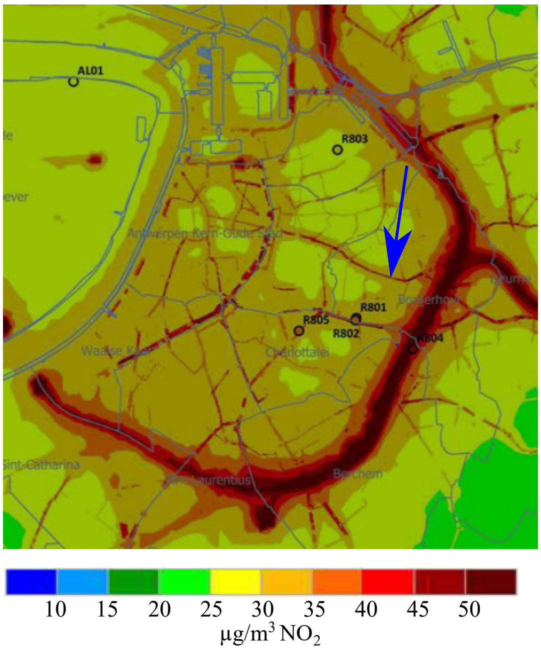

(a) Modeling results for yearly mean NO_2 concentrations in 2018 in Antwerp. The circles represent measurement stations. Adapted from VMM (2019).

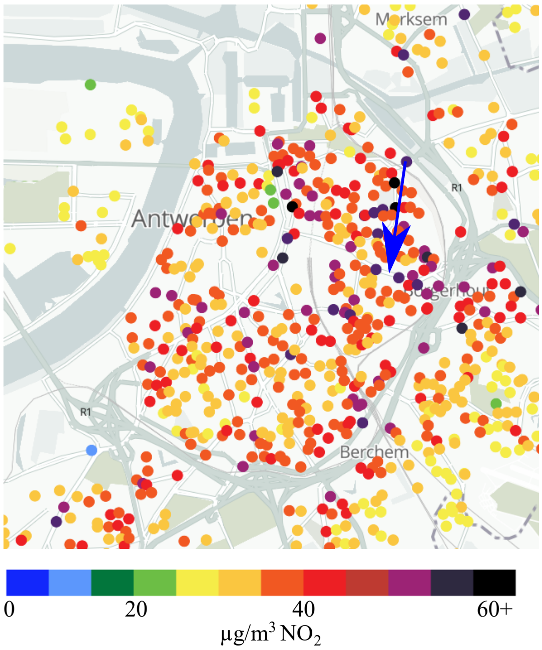

(b) Calculated yearly mean NO_2 concentrations from a one month measurement campaign. Adapted from Meysman and De Craemer (2018).

Figure 1: Location of the Turnhoutsebaan (blue arrow) and air pollution indications in Antwerp (Belgium).

a proper set of realistic inlet conditions and wall functions consistent with the turbulence model is required (Parente et al., 2019).

When dealing with CFD dispersion simulation, a relevant role is played by Sc_t which expresses the ratio of turbulent viscosity to mass diffusivity. The relevance of this parameter in affecting the concentration field is undoubted (Di Bernardino et al., 2019; Gualtieri et al., 2017) and is further demonstrated in the works of different authors (Di Sabatino et al., 2004; Gorlé et al., 2010; Longo et al., 2019). When dealing with atmospheric flows, typical values of Sc_t range between 0.2 and 1.3 (Tominaga et al., 2008). The literature tends to prescribe this parameter as a constant quantity, without reporting a precise and definitive guideline for its specification (Li et al., 2018a; Longo et al., 2019). However, the variable nature of Sc_t has been repeatedly demonstrated (Di Bernardino et al., 2019; Gorlé et al., 2010; Gualtieri et al., 2017; Longo et al., 2019), also referring to a number of experiments (Reynolds, 1975) and to direct numerical simulations (DNS) (Donzis et al., 2014).

2.1. Turbulence and Dispersion modelling

One traditional problem related to ABL simulations lies in the inconsistency between the imposed inlet conditions and the adopted wall treatment (Balogh et al., 2012). This typically results in the rise of horizontal inhomogeneities in the turbulence profiles, as they travel from the inlet to the outlet of the domain. This problem, described in detail by different authors (Longo et al., 2017; Parente et al., 2011a; Pontiggia et al., 2010), can drastically affect the outcomes of the simulation, especially when large domains are involved. To face this issue, a $k-\epsilon$ turbulence closure specific for ABL simulations has been developed (Longo et al., 2017; Parente et al., 2011a), under the hypothesis of steady state, incompressibility, zero vertical velocity, constant pressure along vertical (z) and longitudinal (x) directions, constant shear stress along the boundary layer and no buoyancy effects. This comprehensive approach is suitable for undisturbed flow fields and is based on a consistent deployment of realistic inlet conditions for the main turbulence quantities: a height-decreasing profile for the turbulent kinetic energy, k, and the turbulence dissipation rate, ϵ, and a logarithmic profile for the longitudinal velocity, U. Consequently, the turbulence model parameter C_μ is not kept constant but it is varying with height to locally match the turbulence level (Parente et al., 2011b). Finally, for the sake of consistency, a source term, S_ϵ, is introduced in the turbulence dissipation transport equation (Table 1).

Table 1: Set of inlet conditions and turbulence variables for the "*comprehensive approach*" (Longo et al., 2017, 2019). u_*: friction velocity, κ: von Kármán constant, z_0: roughness length, ρ: air density, μ_t: turbulent viscosity and σ_ϵ, $C_{\epsilon 1}$, and $C_{\epsilon 2}$: $k-\epsilon$ model constants. See text for the other symbols.

Inlet Conditions	**Turbulence Model**
$U = \frac{u_*}{\kappa} ln\left(\frac{z+z_0}{z_0}\right)$	$\mu_t = C_\mu \rho \frac{k^2}{\epsilon}$
$k\left(z\right) = C_1 ln\left(z+z_0\right) + C_2$	$S_\epsilon\left(z\right) = \frac{\rho u_*^4}{\left(z+z_0\right)^2}\left(\frac{\left(C_{\epsilon 2}-C_{\epsilon 1}\right)\sqrt{C_\mu}}{\kappa^2} - \frac{1}{\sigma_\epsilon}\right)$
$\epsilon\left(z\right) = \frac{u_*^3}{\kappa\left(z+z_0\right)}$	$C_\mu = \frac{u_*^4}{k^2}$

For determining the coefficient C_1 and C_2, it is possible to refer to the semi-empirical parameterization proposed by Brost and Wyngaard (1978). Consequently, the variation of turbulent kinetic energy with height can be expressed as:

$$k\left(z\right) = \frac{1}{2}\left(\left\langle u'^2\right\rangle + \left\langle v'^2\right\rangle + \left\langle w'^2\right\rangle\right) = \frac{u_*^2}{2}\left(8.7 - 6\frac{z}{h}\right) \tag{1}$$

where h is the ABL height. For neutral stratification conditions the value of h can be deduced according to Bechmann (2006):

$$\frac{hf_c}{u_*^2} \approx 0.33 \quad (2)$$

where a typical mid-latitude value for the Coriolis parameter, $f_c = 10^{-4}$, is considered (Parente et al., 2011b, 2019).

As for the wall treatment, a wall formulation based on aerodynamic roughness is employed (Balogh et al., 2012; Longo et al., 2019; Parente et al., 2011a). The latter is able to automatically switch between a smooth and a rough treatment.

Whenever obstacles (buildings, trees or hills) are involved, a building influence area (BIA) concept is adopted (Keshavarzian et al., 2020; Longo et al., 2017). The latter permits to automatically detect the obstacle through a deviation parameter δ, estimating the relative error between homogeneous ABL conditions and the local values of relevant turbulence parameters Longo et al. (2020b), as described in Table 2.

Table 2: Formulation of the BIA metric for the blending approaches (Longo et al., 2016, 2020b). The hybrid blending employed in this study consists in selecting the maximum of the three deviations (velocity, turbulent kinetic energy and turbulent dissipation rate).

Pure blending			Hybrid blending
V	TKE	EPS	V & TKE & EPS
$\delta_u = min\left[\left\|\frac{u-u_{ABL}}{u_{ABL}}\right\|, 1\right]$	$\delta_k = min\left[\left\|\frac{k-k_{ABL}}{k_{ABL}}\right\|, 1\right]$	$\delta_\epsilon = min\left[\left\|\frac{\epsilon-\epsilon_{ABL}}{\epsilon_{ABL}}\right\|, 1\right]$	$\delta_h = max[\delta_u, \delta_k, \delta_\epsilon]$

Within this area, specific turbulence closures, suitable for disturbed flow fields, can be applied (Longo et al., 2019, 2020b; Peralta et al., 2014). For this study, the turbulence model selected inside the building influence area (BIA) belongs to the Non-Linear Eddy-Viscosity (NLEV) closures (Craft et al., 1996; Ehrhard and Moussiopoulos, 2000; Lien et al., 1996). These methods extend the Boussinesq hypothesis of the stress-strain relation to higher order terms. In addition, they express C_μ as directly depending on the strain rate invariant S and the vorticity invariant Ω (Longo et al., 2017). These models show a more realistic representation of the normal stresses, an enhanced sensitivity to curvature strain and a more accurate level of turbulence in regions of strong normal straining with respect to the Linear Eddy-Viscosity closures (Craft et al., 1996; Ehrhard and Moussiopoulos, 2000). The specific NLEV closure selected for this study is the one proposed by Ehrhard and Moussiopoulos (2000), whose C_μ reads:

$$C_\mu = min\left(0.15, \frac{1}{0.9S^{1.4} + 0.4\Omega^{1.4} + 3.5}\right). \quad (3)$$

Merci et al. (2004) and Longo et al. (2017) further investigated NLEV models, claiming C_μ to be the most relevant parameter whenever flows characterized by reduced swirl and vorticity are involved. This assumption permits simplifying the NLEV model formulation, neglecting the higher order terms of the stress-strain relation and reducing the computation time.

As for the concentration field, a general equation for the transport of a passive scalar is adopted both for the simulations of NO_2 and PM_{10}. The latter reads:

$$\frac{\partial}{\partial X}\left(\bar{U}\bar{C} - (D_m + D_t)\frac{\partial \bar{C}}{\partial X}\right) = \bar{\dot{C}}_0, \tag{4}$$

where $\bar{C}$ is the solute concentration, $D_m = \nu/Sc$ is the molecular diffusion coefficient and $D_t = \nu_t/Sc_t$ is the turbulent diffusion coefficient.

The deployment of this approach also for the dispersion of particle matter is an acceptable assumption, considering that validation studies involving gases are good indicators of the performance of the model in terms of calculations of particle mass concentrations (Holmes and Morawska, 2006). Moreover, air quality regulations are currently based on particle mass concentrations (Blocken et al., 2016). Finally, the computation time required by the passive scalar approach is shorter than the Eulerian-Lagrangian one, up to 5 times (Pospisil and Jicha, 2010).

The standard gradient diffusion hypothesis (SGDH) is applied and Sc_t, a relevant dispersion parameter usually expressed as a constant property (Longo et al., 2018), is defined as locally variable, according to the formulation proposed by Longo et al. (2020a). This Sc_t formulation, accounting for most of the experimental observations and numerical evidences, is capable of enhanced accuracy with respect to the standard methodologies (Longo et al., 2019, 2020a). It is expressed by the following relation:

$$Sc_t = exp\left(a\ Sc - b\ Re_{turb}^c - d\ S - e\ \Omega\right) \tag{5}$$

where Sc is the molecular Schmidt number, Re_{turb} is the turbulent Reynolds number, S and Ω are the strain rate and vorticity invariants respectively. The a, b, c, d coefficients are specified in Table 3 (Longo et al., 2020a).

Table 3: Coefficients for the variable turbulent Schmidt number, Sc_t, formulation, directly depending on relevant turbulence quantities.

a	b	c	d	e
0.6617	0.8188	0.01	0.0031	0.0329

2.2. Turnhoutsebaan: site location, data and measurements

2.2.1. Site location

The Turnhoutsebaan is a main artery street in the city of Antwerp (Belgium, Figure 1(a)). It was selected as a case study, due to its problematic air pollution levels (Figures 1 (a) and(b)). It is necessary to investigate the spatial distribution of air pollution on a fine spatial scale, as argued in Section 1.1. Therefore, a CFD model of a part of the Turnhoustebaan was made (Section 2.4), since CFD models indeed deliver such detailed spatial resolutions (Moonen et al., 2012) and because CFD is considered as powerful instrument to predict dispersion patterns in complex urban environments (Section 2). Measurements at the Turnhoutsebaan site were made (Sections 2.2.5 and 2.2.6), to validate the model. Mitigation measures were implemented in the model at detected pollution hotspots (Section 2.5).

2.2.2. Selected meteorological conditions

For the proper specification of the boundary conditions, information about the local meteorological conditions is required. In this study, wind directions are expressed in degrees, where 0° corresponds to a wind direction blowing from the North, 90° from the East, 180° from the South, and 270° from the West. Measurement data of the wind for the entire year 2017 were obtained from a weather station of the Flanders Environment Agency (VMM). The latter, located in Antwerp at approximately 5.3 km from the modeled site (coordinates: 51° 15’ 39.56" N 4° 25’ 27.84" E), measures at a height of 30 m, and delivers data each 30 minutes. Histograms to determine the probability of specific wind speed and direction values are shown in Figure 2.

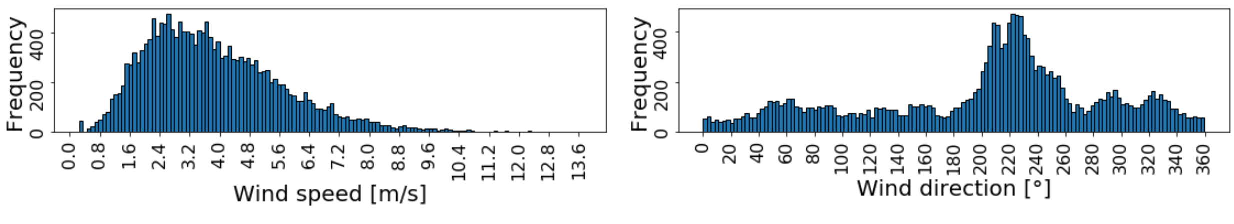

Figure 2: Histograms of the wind speed and the wind direction in Antwerp in the year 2017 as measured by the VMM weather station.

The meteorological conditions selected for the simulation session consist of a wind direction of 202.5°, with a reference wind speed of 3.55 m/s as measured by the VMM station, and a neutrally stratified atmosphere. This specific wind condition was chosen, considering its relatively high frequency. Moreover, in street canyon configurations, including the one under study, wind direction perpendicular to the main street orientation can cause an internal clockwise vortex (Figure 28), typically resulting in a slower dilution process and, consequently, in a concerning scenario (Arkon and Özkol, 2014; Dabberdt and Hoydysh, 1991; Huang et al., 2019; Xie et al., 2009; Yassin, 2013; Zhang et al., 2016).

2.2.3. Traffic data and pollutant emissions

In Section 1.1, the relevance of the health effect of NO_x and PM in the ambient air and the contribution of traffic to their emissions was already explained. This study has a number of goals which are somewhat diverse (Section 1.3). Therefore, to keep the results and discussion section of this paper concise, NO_2 and PM_{10} were selected from NO, NO_2, $PM_{2.5}$, and PM_{10} as pollutants to be modeled, lowering the number of scenarios that needs to be analyzed. NO_2 and PM_{10} are selected from the viewpoint of legislation. In the European law, NO_2 has and NO does not have limit values related to human health issues EU (2015). Regarding PM_{10} and $PM_{2.5}$, PM_{10} has a limit value for 24 hour average values, $PM_{2.5}$ has only a limit value for yearly averaged values. The CFD model results of this study are not representative for yearly averages. The model delivers steady state results which are probably representative for averages over shorter periods. Hence, selecting NO_2 and PM_{10} allows to compare the results to the European legislation. In addition, indications have been found that NO_2 is suitable as proxy for traffic-related air pollutant concentration levels of other compounds, e.g. NO Beckerman et al. (2008). With regard to PM_{10} and $PM_{2.5}$, it was already observed that the transport of particles with a 10 and 2.5 µm diameter is very comparable at higher air speeds, but can show differences at lower air speeds Vervoort et al. (2019). Therefore, a more complete analysis of air pollution at the Turnhoutsebaan should involve both substances. The goal of this study is however only to discover whether relevant pollutant concentration patterns emerge at detailed spatial scales, for which modeling only PM_{10} was sufficient. It was, in addition, already observed, that correlations between PM_{10} and $PM_{2.5}$ concentrations on 5 urban sites across Europe were very high ($R^2 \geq 0.98$) Van Dingenen et al. (2004).

To quantify traffic emissions of NO_2 and PM_{10}, traffic count data for the Turnhoutsebaan was obtained from the municipality of Antwerp (Figure 3). Traffic was counted in the Turnhoutsebaan section between Laar and Drink, the two side streets at the downwind side of the Turnhoutsebaan included in the computational domain (Figure 4). Traffic lane A, highlighted in green, is towards the city center, while lane B, evidenced in blue, points to the outskirts. Hourly observations are available, for lane A from 26 September

2014 to 23 October 2014, and for lane B from 26 September 2014 to 30 October 2014. Furthermore, data is available for different vehicle types, including the categories car, bus, truck<20 metric ton and truck>20 metric ton. For each vehicle type, the mean, median and standard deviation of the observed vehicle numbers were calculated per hour over all available days (see Figure 3, representative for the car data). Since it was observed that outliers in the vehicle numbers occur, the median was chosen instead of the mean as statistic to serve as input data for the model. The selected time slot for the simulation is [17h-18h[, considering that traffic intensity is expected to be very high, corresponding again to a very problematic scenario.

The conversion of vehicle numbers to pollutant emissions was performed referring to the emission factors

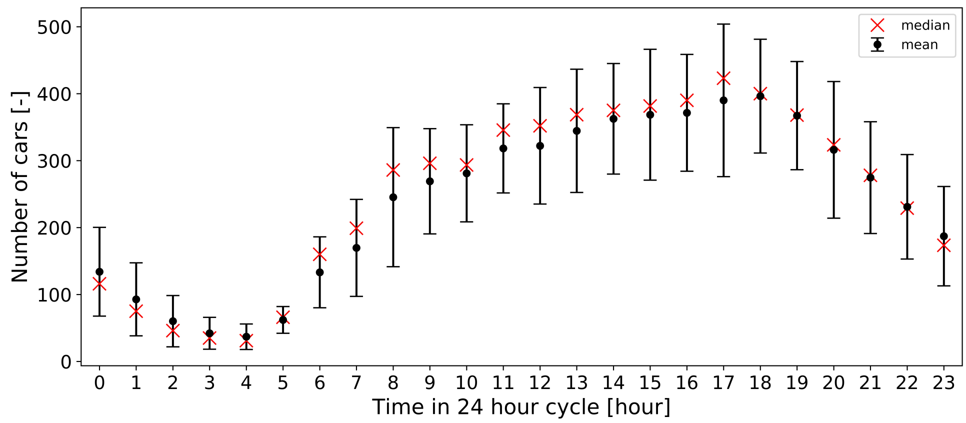

(a) Number of cars in traffic lane A (Figure 11(b)).

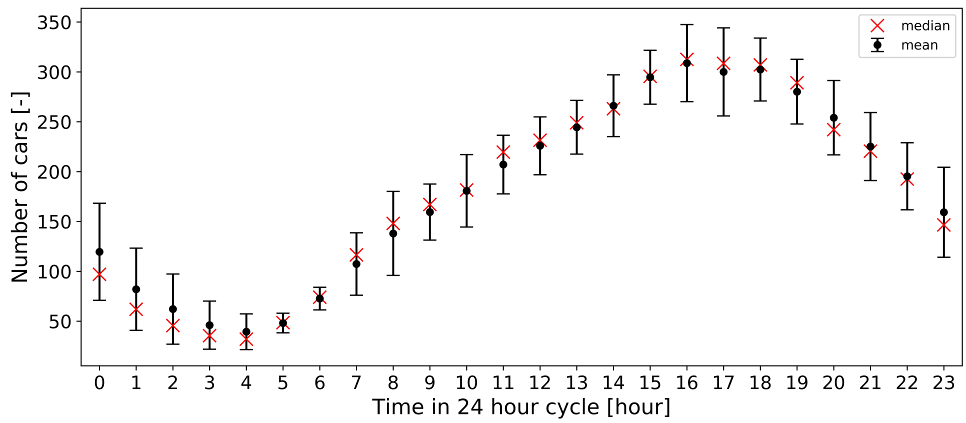

(b) Number of cars in traffic lane B (Figure 11(b)).

Figure 3: Average and median of number of cars per hour over all observation days of the used traffic count data. Data points are valid within the time interval starting from their abscissa until - but not including - the next. The error bars show the standard deviation, not the standard error of the mean, to illustrate the variation in the data.

of the Dutch government for 2017 (Rijksoverheid, 2018). “City stagnating” (in Dutch: “stad stagnerend”) is the traffic and road type, which was selected from the emission factor data. The emission factors have the units g/km. Thus, the number of vehicles within each category was converted to driven km. Two traffic lanes were assumed (each side has two lanes, of which just one is heavily used). The length of each lane in the model was estimated as 668 m. Thus, per direction and vehicle category, the number of vehicles was multiplied by 0.668 km to finally retrieve the number of driven km in the modeled part of the Turnhoutsebaan. The number of driven km per vehicle type was multiplied by its corresponding emission factor, to obtain the emitted pollutant mass per vehicle type and per traffic lane, during one hour, analogously to Blocken et al. (2016) (See Table 4 for a summary of the traffic data). Per traffic lane, the emitted pollutant masses per hour for all vehicle types were summed together. This resulted in 42.97 g NO_2 h^{-1} and 14.16 g PM_{10} h^{-1} for lane A and 27.23 g NO_2 h^{-1} and 8.88 g PM_{10} h^{-1} for lane B.

Table 4: Summary of traffic data used in the Turnhoutsebaan model (Section 2.4). See text for vehicle number to emission conversion method. NO_2 emissions included as example. EF: emission factor.

	EF NO_2 [g/km]	EF PM_{10} [g/km]	Lane A, number [-]	Lane B, number [-]	Lane A, NO_2 emission [g/h]	Lane B, NO_2 emission [g/h]
car	0.11845	0.0382	423	308	33.47	24.37
bus	0.6625	0.18845	3	1	1.33	0.44
truck<20 ton	0.5449	0.21345	7	3	2.55	1.09
truck>20 ton	0.6476	0.2302	13	3	5.62	1.30

2.2.4. Estimation of the pollutant background concentration

Figure 4 shows the locations in Antwerp of measurement stations R801 and R802 of the VMM. Data of NO_2 and PM_{10} concentrations was obtained for 2017 (time series of 30 min averages). The data of these stations was used to estimate the urban background concentration at the Turnhoutsebaan and to perform a rough validation of the increased concentration due to traffic emissions in proximity of the road artery. The concentration flowing into the Turnhoutsebaan with the wind is the definition of background concentration used in this work. The expected background concentration in the Turnhoutsebaan model (Section 2.4) is set by imposing the proper pollutant mass fraction entering the inflow of the computational domain (Figure 11(a)).

To estimate the background concentration, the available measurements were averaged at specific wind directions and other meteorological conditions. Said meteorological data was retrieved from the station described in Section 2.2.2 and from the station of the Royal Meteorological Institute of Belgium in Deurne. For a wind direction $\in$ [315°, 360°] or [0°, 67.5°], and time $\in$ [15 h, 20 h], the average obtained from station R801 at aforementioned meteorological conditions is assumed to be representative for the background

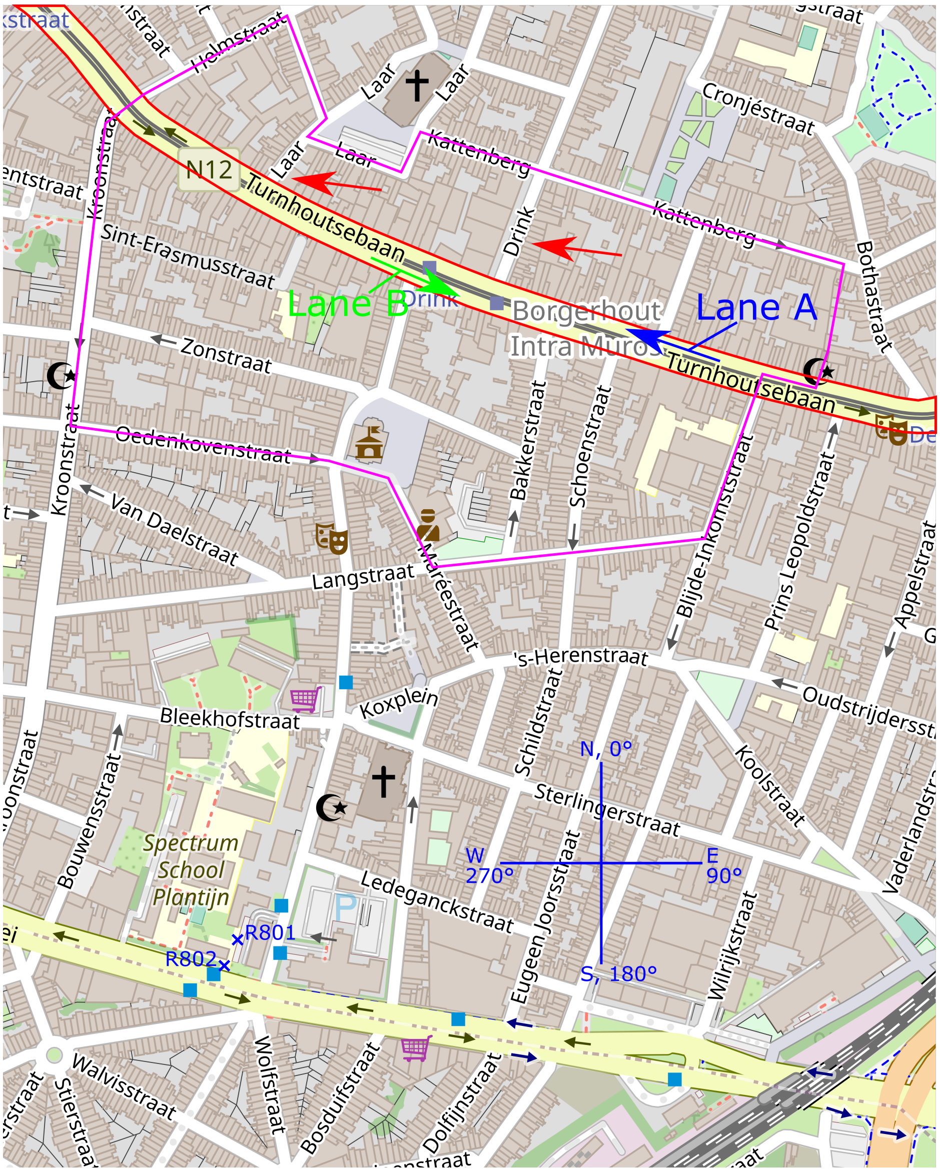

Figure 4: Modified from OpenStreetMap (2019). The license of OpenStreetMap® applies to the modified figure. Locations of VMM measurement stations R801 and R802. Station R802 measures pollutants at a height of approx. 3 to 4 m. Red polygon: Turnhoutsebaan. Red arrows: side streets of the Turnhoutsebaan, Laar and Drink. Blue and green arrows: lane towards the city center and the outskirts respectively. Purple polygon: area around the Turnhoutsebaan where the buildings are explicitly modeled in the used CFD model (Figure 11).

concentration used in the model. This wind direction is argued to be representative for the background concentration, because in this case the wind is not transporting pollutants directly from a major road towards the station (Figure 4). This resulted in an NO_2 concentration of 35.54 µg/m^3 (standard deviation: 11.82 µg/m^3) and a PM_{10} concentration of 26.04 µg/m^3 (standard deviation: 18.38 µg/m^3). For the increased concentration due to traffic emissions nearby the road, a wind direction $\in$ [135°, 225°] was used to select data from station R802, because in this case the wind is transporting pollutants directly from a major road towards station R802, which is located very close to the road. This resulted in a PM_{10} concentration of 25.39 µg m^{-3} (standard deviation of 13.58 µg/m^3) and a NO_2 concentration of 62.47 µg/m^3 (standard deviation of 16.77 µg/m^3). Figure 5 shows all observed NO_2 concentrations during the meteorological conditions used for the background concentration (data from July and August was excluded from the average because of the summer vacation).

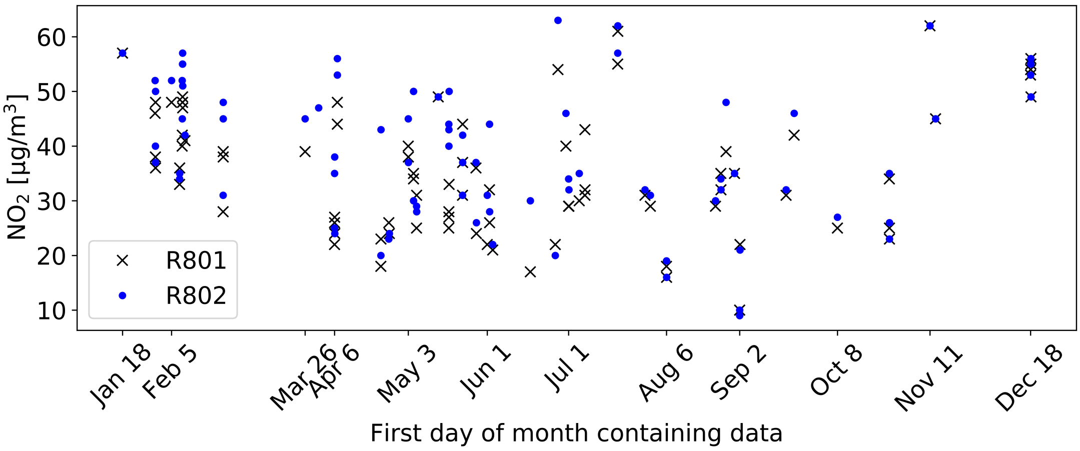

Figure 5: Concentrations measured by VMM stations R801 and R802 (Figure 4), occurring at the meteorological conditions representative for the background concentration.

2.2.5. Wind measurements in the domain of interest and data processing

Figure 6 displays the locations within the Turnhoutsebaan where the wind xy velocity magnitude and direction were measured during the day (9am-18pm), from 27 January to 31 January 2020. The xy velocity magnitude is the velocity magnitude in the xy plane (horizontal plane), defined according to: $U_{xy} = \sqrt{u_x^2 + u_y^2}$. Measurements were performed and logged every 10 s with the KWS1 cup anemometer and the PCE-WL 1 data logger of PCE instruments. The accuracy of the wind speed measurements was $\pm$ 0.5 m/s or 5 % of value (largest value applies), while the accuracy of the direction was $\pm$ 5°. The starting threshold value for valid measurements is 0.8 m/s. The removal of values below the starting threshold from the data sets was considered. However, after careful visual inspection of the consequences of using a number of different removal thresholds, it was decided that keeping most data points was a reasonable choice. No velocity values were removed from the data set. Wind direction values occurring at time instants where the velocity was below 0.2 m/s were removed. Missing wind direction values were obtained by linearly interpolating the remaining data.

Measurements were performed with a strategy similar to the one adopted by Tominaga et al. (2008). One anemometer was set as base instrument, at approx. 1.5 m above the roof of the tallest building in the modeled part of the Turnhoutsebaan (building height in the model = 31 m), to determine the undisturbed wind conditions. The other anemometer was then displaced in strategic locations inside the urban canyon, recording data at a height of approx. 1.43 m, when the base anemometer was detecting the aimed wind direction, i.e. corresponding to the inflow used (Section 2.2.2) in the Turnhoutsebaan model (Section 2.4). Correspondence of the roof data to the used inflow direction (202.5°) during the measurements used to calculate the average street wind directions was good. Average directions at the roof were e.g. 180.8°, 202.4°, and 223.9°. In total, measurements in the Turnhoutsebaan were achieved in 6 different locations. Per location, the average and the standard error of the mean were calculated. Long averaging periods, ranging from 46 min to 172 min, were used for the velocity angles. The velocity magnitude at the roof during the measurement campaign was too high and also very variable (see Figure 7). To compensate the first problem, in the street data sets where the roof direction again corresponded well to the model inflow direction, periods characterized by a low velocity at the roof were selected (e.g. the period where approximately time $\in [136, 172]$ min in Figure 7). This, however, resulted in short averaging times for the velocity magnitude in some cases, where these averaging times range from 4 min to approx. 160 min. To overcome the model validation problem due to variability in the inflowing wind, it will be meaningful in the future to model combinations of several wind directions and speeds. In this way it will be very likely that measurements will be registered where the conditions are very close to inflow conditions used in the model, during sufficiently long periods.

Velocity

No.	x(m)	y(m)	z(m)
1	-6.60	62.07	1.43
2	-8.03	-45.82	1.43
3	-3.43	-96.63	1.43
4	11.56	-98.54	1.43
5	-0.07	-146	1.43
6	6.15	-206.48	1.43

Concentration

No.	x(m)	y(m)	z(m)
1	-6.60	62.07	1.43
2	10.60	-85.26	1.43
3	-3.43	-96.63	1.43
4	11.56	-98.54	1.43
5	-0.07	-146	1.43

Figure 6: Location and numbering of available experimental data of wind velocity and direction (highlighted in red), and PM_{10} concentration (highlighted in green), in the Turnhoutsebaan. The base anemometer (B.A.) is indicated in light blue, at coordinates ($x = -17m$, $y = -151m$, $z = 32.5m$).

Figure 7: Wind velocity direction and xy magnitude measured at the roof, during the period when the wind in location 3 (Figure 6) was measured.

2.2.6. PM$_{10}$ concentration measurements in the zone of interest and data processing

PM$_{10}$ was measured with a DustTrak II, model number 8530 (aerosol concentration range 0.001 to 400 mg/m^3), using a PM$_{10}$ impactor. Five key locations were considered within the urban canyon (Figure 6). Figure 8 shows an example of measurements made during 1 hour at location 1. It is clear that at approx. time = 2250 s, a drop in the concentration occurs. For this reason, averages of PM$_{10}$ were made of time spans from the data sets, where the average concentration was approximately constant. The used averaging times ranged from 20 to 38 min. The standard error of the mean was also calculated. During the PM$_{10}$ measurements, the total numbers of vehicles were counted, which ranged from 570 to 834 vehicles/h in the used data sets (number used in the model: 761, Table 4).

The concentration entering the Turnhoutsebaan with the incoming wind is the definition of background concentration used in this work. Based on the aforementioned observation that the PM$_{10}$ concentration can clearly vary in a short time span (Figure 8), it is obvious that it is necessary to measure a location in the street at the same time when measuring the concentration flowing into the Turnhoutsebaan, to properly know the background concentration. However, only 1 DustTrak was available. Hence, the background had to be estimated. This is something that needs to be improved in future work. The estimation was performed based on 2 different sources: 1) from short measurements in an upwind side street, before and/or after a location was measured, and 2) from VMM measurement stations R801 and R802 (Figure 4) and R803 located in Park Spoor Noord (Figure 1 (a)).

During the campaign, the observed values used to estimate the background concentration were variable and never equal to the used background concentration in the model. Therefore, in the comparison of the modeled and measured concentrations, the difference between the concentration and the background concentration is used. The errors for these values were computed through error propagation.

For multiple locations, multiple data sets are available. Considering all available data - wind velocity magnitudes and directions at the street locations and the roof, numbers of vehicles, and different background concentration estimations - the pollution measurements performed during conditions corresponding best to the conditions used in the model were selected.

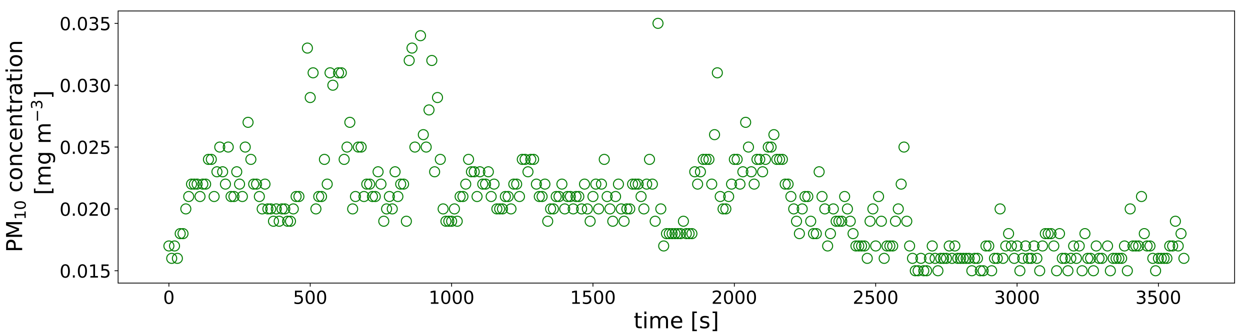

Figure 8: Time series of PM$_{10}$ measurements performed at location 1.

2.3. Modeling method validation on idealized street canyon wind tunnel data

The scaled model street canyon from the CODASC dataset (Karlsruhe Institute of Technology, n.d.) consists of an empty urban canyon, perpendicular to the inlet velocity, as shown in Figure 9. Its dimensions are specified in Figure 9 (b), with the distance D between the two internal facades (wall A upwind and wall B downwind) equal to the length L and to the height H of the building, $D = L = H = 0.12$ m. The origin of the coordinate system is set at the center of the street canyon. The width of the building, in the y direction, measures $W = 1.2$ m. The pollutant is emitted from 4 line sources, each of them is 1.42 m long. The dimensions of the computational domain are 4.92 m, 2 m and 1 m in the x, y and z directions. The inlet is set $8H$ upstream of the first building (building A) and the outlet is located $30H$ downstream of the downwind building (building B). The 4 source lines are modeled as mass-flow inlet, with $Q = 0.02$ kg/s. z_0, the roughness length, and u_*, the friction velocity, were specified equal to 0.0033 m and 0.535 m/s respectively. A structured mesh consisting of 3.5 million hexahedral cells was generated. A grid sensitivity analysis was already carry out by Longo et al. (2020a). As a consequence, the mesh is considered reliable. This specific case was selected for validation, representing an idealized urban canyon, with an orientation analogous or similar to the one considered for the Turnhoutsebaan case study.

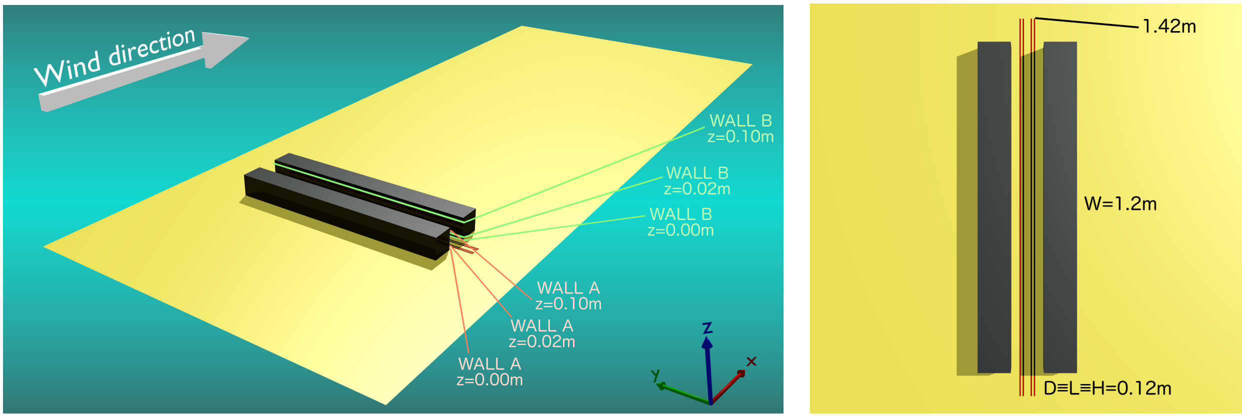

(a) (b)

Figure 9: CODASC empty street canyon test case view, dimensions and measuring lines (a). Four line sources are located on the ground, in-between the buildings (b) (Longo et al., 2020a).

Results for this first simulation are shown in Figure 10. Analogously to Longo et al. (2020a), the experimental data are compared with the outcomes of the ABL modeling approach coupled to the proposed variable Sc_t and the standard $k-\epsilon$ model with a constant $Sc_t = 0.4$. Additionally, the realizable $k-\epsilon$ model coupled with both $Sc_t = 0.3$ and $Sc_t = 0.7$ were studied and added to the graphs. The latter were selected for comparison, as they are modeling configurations traditionally employed in ABL dispersion literature (Blocken et al., 2016; Di Sabatino et al., 2004). Considering the symmetry of the problem, only half of the concentration profiles (-0.6 m $< y < 0$ m) are considered. The concentration is expressed in dimensionless form, according to:

$$K = \frac{x_i U_{ref} H}{Q_l} \tag{6}$$

with x_i, the measured tracer molar fraction; U_{ref}, the reference wind speed in m/s; H, the building height (0.12 m); and $Q_l \equiv Q/L$, the emission rate of 1 line source in m^2/s.

In this kind of street canyon configuration, with the wind direction perpendicular to the orientation of the canyon, a clock-wise vortex originates (Gromke et al., 2008; Oke, 1988), leading to a lower dilution process, to the gathering of the pollutant inside the urban canyon, and to higher concentrations on the internal upwind facade (wall A). It can be noticed that the variable Sc_t number permits an increase in the accuracy of the predictions in almost all the considered locations, both on the facades of building A and B, with respect to the standard approaches. The trend of both the standard $k - \epsilon$ (dashed green line) and realizable $k - \epsilon$ (blue rhombus and light blue triangles) is that of overestimating the concentration field, especially when approaching the central locations of the street canyon (-0.3 m $\times\, y \times 0$ m). The highest discrepancies, on a larger number of locations, can be witnessed for the standard $k - \epsilon$ model. A less erroneous behavior is shown by the realizable model. In particular the simulation with $Sc_t = 0.7$ approaches the ABL modeling results on facade B, with just a light overprediction of concentrations. However, a larger inaccuracy is shown on facade A, also in the most external locations (-0.6 m $< y < -0.25$ m), where, differently from more central locations, the realizable configuration with $Sc_t = 0.3$ predicts more accurately the concentration. As previously mentioned, the ABL model coupled with a variable Sc_t formulation shows, in general, improved accuracy. Few discrepancies can be witnessed also at the central locations of the street canyon, with a slight overprediction of the concentration. This validation study further demonstrates that the Sc_t plays an important role in the concentration field and that a good agreement with experimental data is hardly achievable with the employment of a constant Sc_t.

An assessment of the turbulence quantities at the inlet and outlet of the domain demonstrated the absence of horizontal inhomogeneities in the profiles of velocity, turbulent kinetic energy and turbulence dissipation rate for the ABL turbulence model, as demonstrated in previous publications (Longo et al., 2017, 2020b).

The proposed turbulence and dispersion methodologies were already successfully validated by Longo et al. (2020a) over two supplementary test cases: an isolated single building and an array of buildings. Consequently, the ABL modeling approach coupled to the variable Sc_t formulation from Eq. 5 was selected for the simulation campaign on the Antwerp test case.

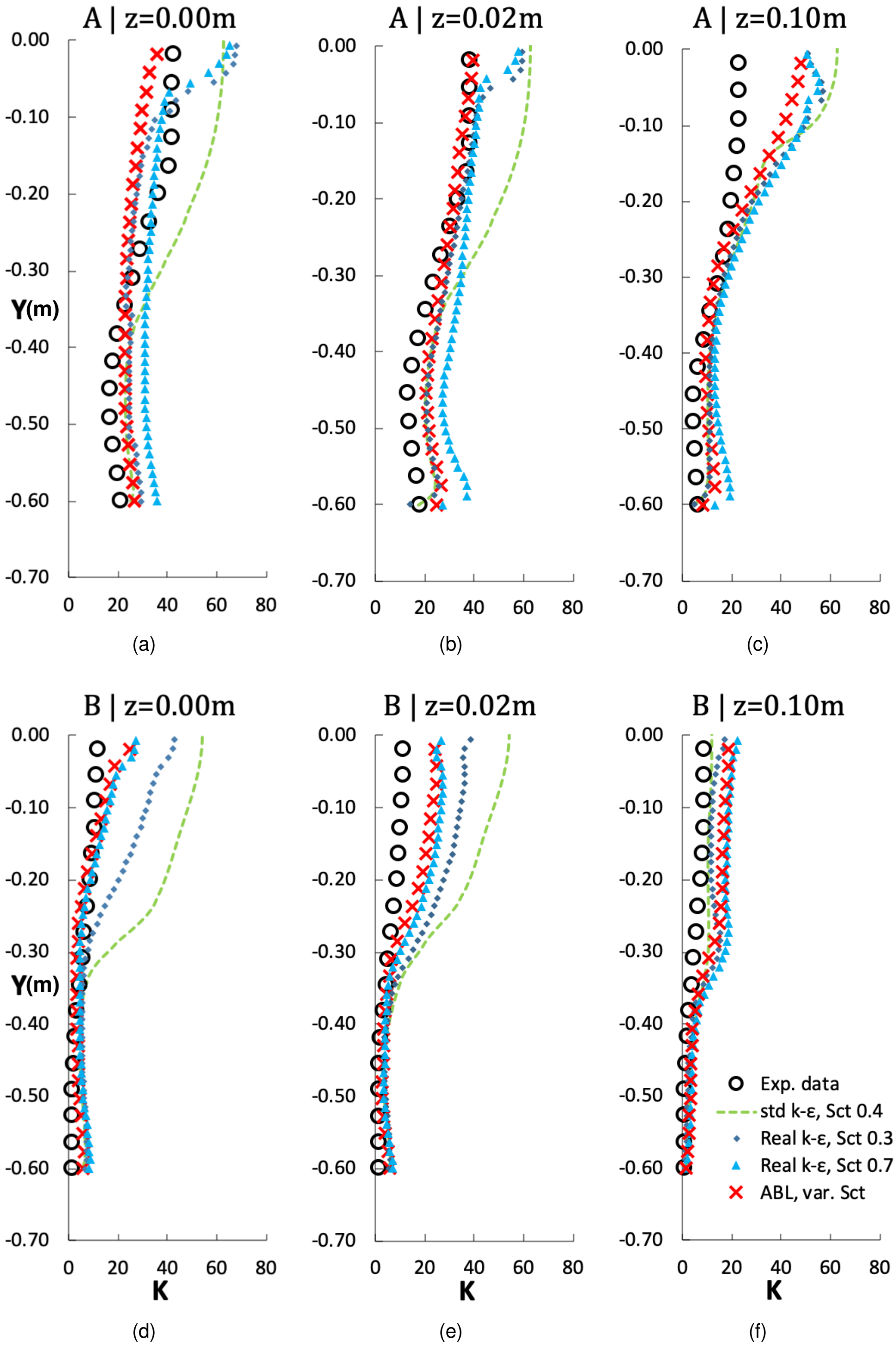

Figure 10: Comparison of experimental and numerical predictions of non-dimensional concentration K for the empty street canyon test case at different horizontal axial locations (Figure 9), using the standard $k-\epsilon$ with $Sc_t = 0.4$ (green dashed line), the realizable $k-\epsilon$ with $Sc_t = 0.3$ (blue rhombus), the realizable $k-\epsilon$ with $Sc_t = 0.7$ (blue triangle), and the ABL turbulence model with variable Sc_t formulation (red cross)."A" stands for "wall A" (the upwind internal facade) while "B" stands for "wall B" (the downwind internal facade).

2.4. Turnhoutsebaan model: computational domain, settings, and grid

Figure 11 displays the geometry and the extent of the computational domain of the Turnhoutsebaan. The geometry drawing stemmed from a 2D plan of the land lots in Antwerp. The third dimension was added, based on information of a website of the Flemish government (Vlaamse overheid, 2019), Google Earth and Google Maps. A combination of the three mentioned sources together with in-place inspections were used to carefully estimate the 3D building dimensions and the street configuration.

As shown in Figure 11 (a), the guidelines on the extent of the domain and the minimum distances from the boundaries were respected (Franke et al., 2007; Tominaga et al., 2008). The overall dimensions of the domain were 1050 m, 1000 m and 400 m in the x, y, z directions respectively. The inlet, modeled as velocity inflow was placed at more than $5H_{max}$ (where $H_{max} = 32$ m is the height of the tallest building inside the computational domain) from the first building. The inlet profiles from Table 1 were employed for the turbulence quantities and the velocity, where z_0, the roughness length, was estimated as 0.65 m and u_*, the friction velocity, calculated as 0.3777 m/s. The end of the domain, at $15H_{max}$ from the last building, was modeled with a pressure outlet condition. Both lateral sides, at $5H_{max}$ from the lateral buildings, were modeled imposing a symmetry condition. The top boundary was set as inlet velocity too, with a x-direction velocity computed from the logarithmic profile at the top height. The ground was treated as a rough wall with z_0 estimated as 0.65 m, while the buildings and the main street were modeled as smooth walls. The Turnhoutsebaan has two traffic lanes in each direction, but one of them is for public transport and is less frequently used. Therefore, only 1 lane in each direction was assumed. The two lanes were treated as emitting surfaces, with the following estimated pollutant mass flow rates: 42.97 g NO_2 h^{-1} and 14.16 g PM_{10} h^{-1} for lane A; 27.23 g NO_2 h^{-1} and 8.88 g PM_{10} h^{-1} for lane B (Section 2.2.3). Finally, 35.54 µg/m^3 and 26.04 µg/m^3 were imposed as background concentration for NO_2 and a PM_{10} respectively (Section 2.2.4).

As for the computational grid, it consists of approximately 35 million hexahedral elements. The grid is finer in the area of interest (namely close to the source lanes, in the main street canyon, around the surrounding buildings) and towards the ground boundary. In the main urban canyon (namely, in the Turnhoutsebaan), an average wall dimensionless distance $y^+ = 290$ is reached. A grid sensitivity analysis was carried out, building one finer grid with a refinement ratio $r_h = 1.18$, resulting in nearly 56 million cells. For the grid sensitivity analysis, the relative errors of U and k were estimated equal to 0.4 % and 0.5 % respectively. When comparing two meshes instead of three, a conservative safety factor is usually advised (Roache, 1998, 2009), namely $F_S = 3$, to calculate the grid convergence index (GCI). A GCI of 3 % was determined

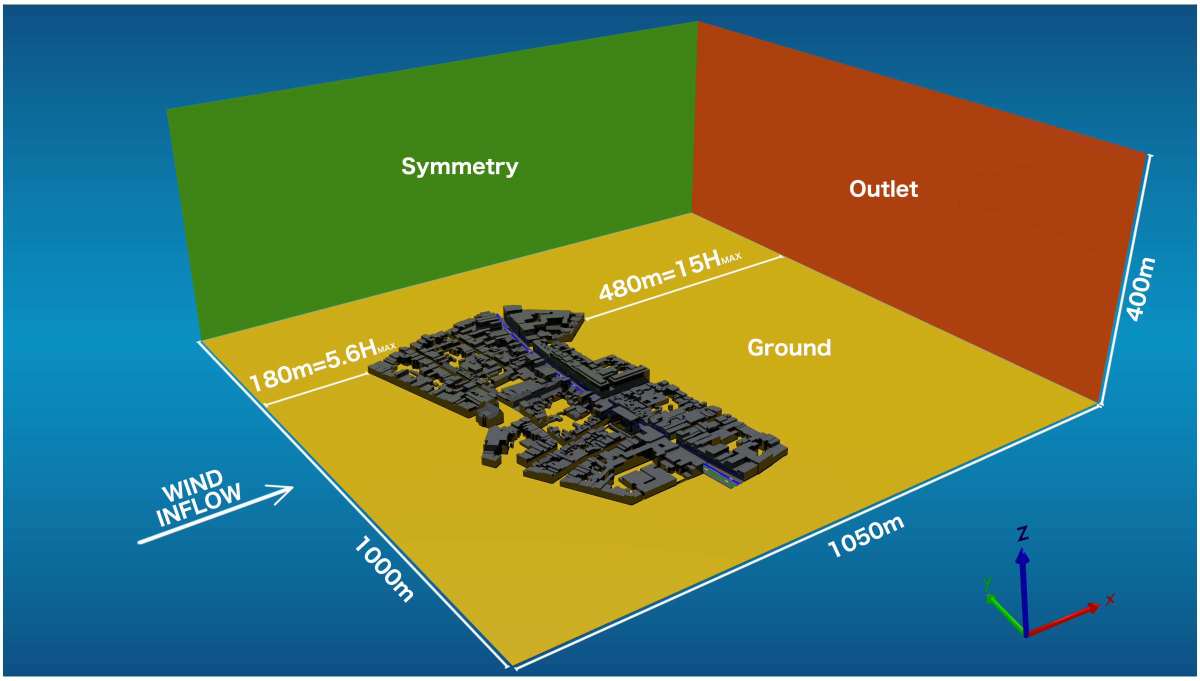

(a) CAD model, computational domain extent and boundary conditions adopted. $H_{max} = 32$ m is the height of the tallest building within the considered district.

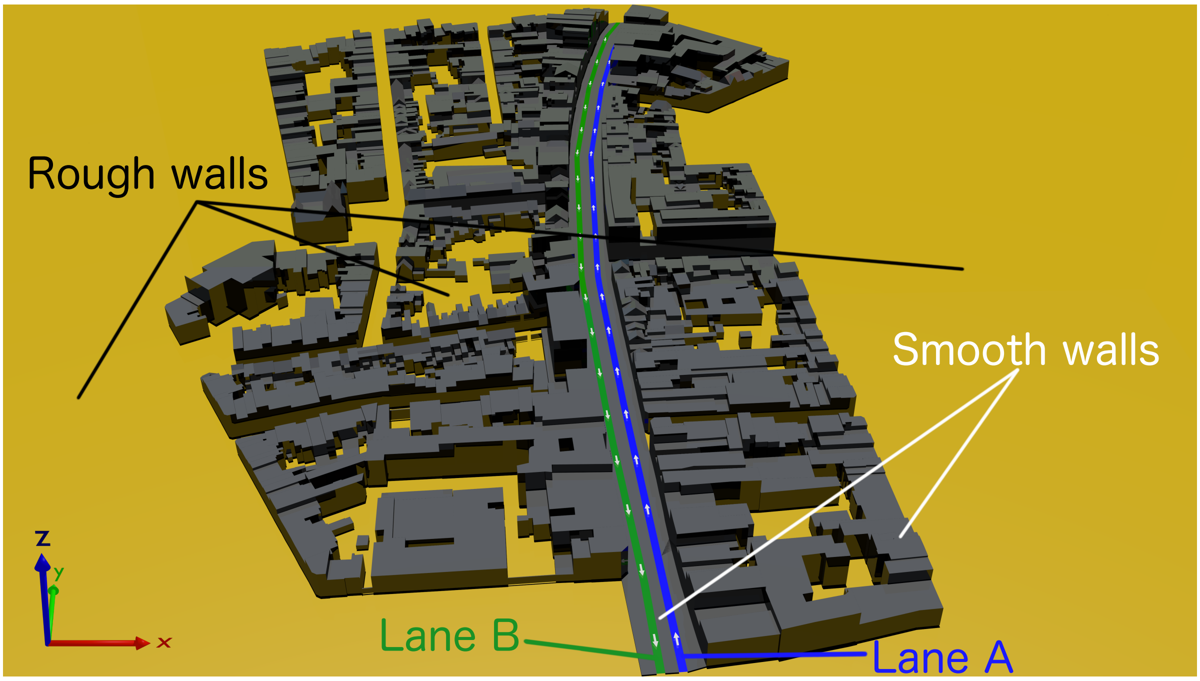

(b) View of the considered Antwerp district around the Turnhoutsebaan, with lane A (towards the city center) displayed in blue and lane B (towards the outskirts) displayed in green. The Turnhoutsebaan street and the surrounding buildings are treated as smooth walls. The surrounding ground and the areas enclosed by the building blocks are modeled as rough walls.

Figure 11: Zone of interest, domain extent and CAD model of the Turnhoutsebaan.

for the velocity and of 4 % for the turbulent kinetic energy, with respect to the finest grid. The computational grid is shown in Figure 12, with its distribution displayed for all the domain and at some strategic locations. The simulations were run in ANSYS Fluent 2019 R3. Second-order schemes were set for the momentum, turbulence quantities and the solute concentration, with a coupled scheme for pressure and velocity. Convergence was assumed to be reached when the scaled residuals leveled down to a minimum of 10^{-9} for species concentration and x-, y-, and z-velocity, 10^{-7} for k, and 10^{-6} for continuity and ϵ.

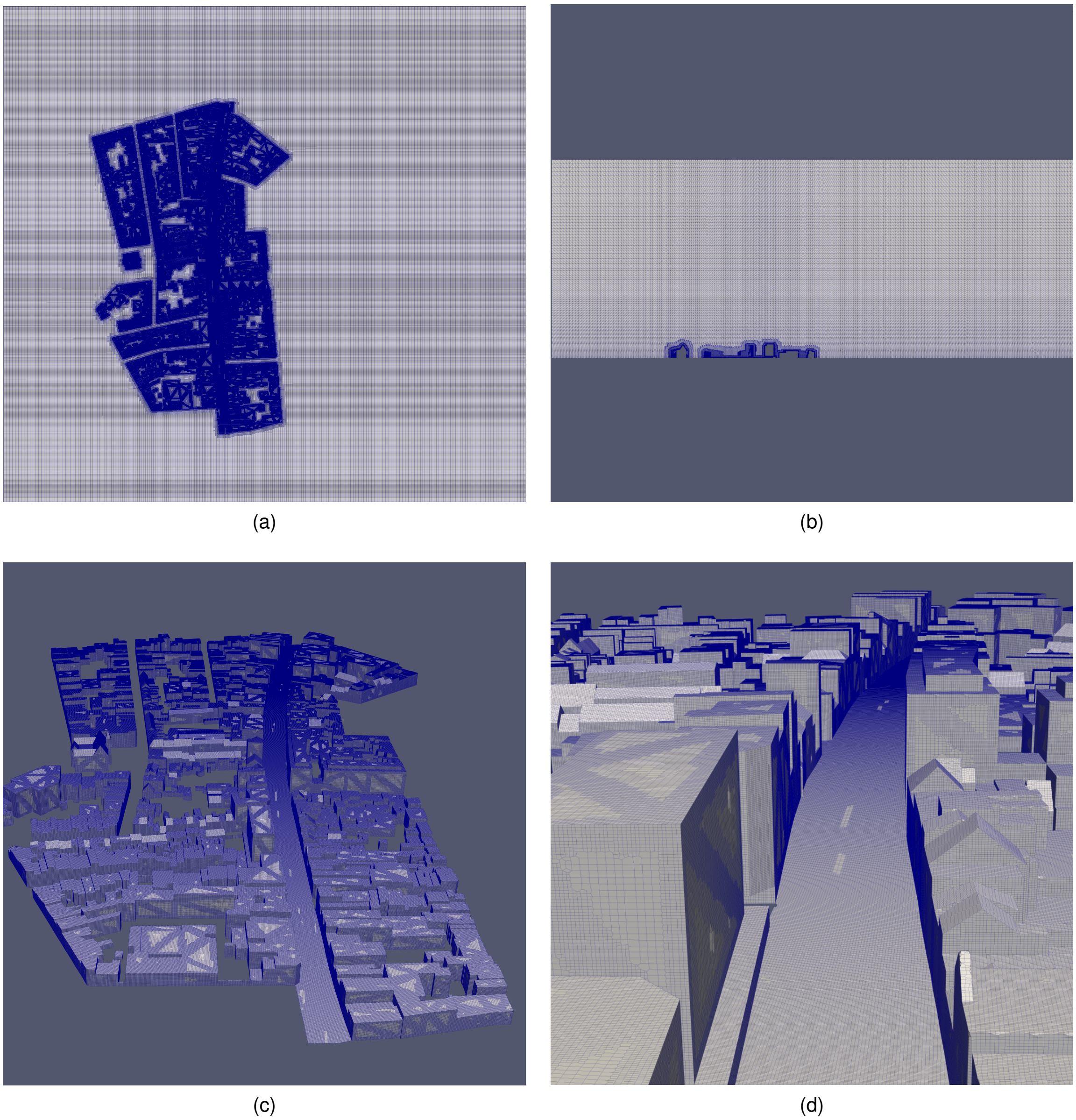

Figure 12: Computational mesh of the Antwerp case study on the ground and city district (a), on the vertical symmetry plane (b), on the buildings composing the Turnhoutsebaan (c), and on the main street (d). The grid is finer towards the city and close to the ground boundary. A high degree of refinement is applied for the street lanes and for the whole street canyon, which are the main subjects of this study.

2.5. Conceived and simulated local mitigation measures

Both the literature (Section 1.1) and model results of this research (Section 3) indicate that air pollution distributions in urban areas can be strongly heterogeneous. In this study, for example, localized pollution hotspots in the modeled street canyon were identified (Figure 22 (a), (b), and (c)), which are caused by a lower natural ventilation rate at locations where high buildings are obstructing the wind flow and causing recirculation areas (Figure 19(b)). Therefore, the effect of applying local mitigation measures to lower pollution levels at the identified localized hotspots was assessed. An additional goal in employing these measures, was to find solutions that can be applied realistically in an existing urban area. In this section, the adopted mitigation measures will be introduced and described.

In Section 1.2, available local mitigation measures were discussed. Two possibilities, designing and modifying the local urban geometry and removal by ESP, were selected and the reasons for this choice were discussed.

With regard to the first measure, altering the urban geometry to enhance natural ventilation and dilution of pollutants was identified as an interesting strategy. Evidently, this measure can be applied to both PM and NO_x. Relevant literature covering a broad range of possible geometric designs and modifications is presented in Section 1.2. However, applying such measures in an existing situation limits the number of possibilities. For example, making one floor in a building permeable to the wind (Zhang et al., 2019) would mean evicting the current residents; and altering the orientation of a street relative to the prevailing wind direction (Voordeckers et al., in press), or the building height variation, or street width (Hang and Li, 2010) is impossible in an existing urban quarter. Besides, looking at Figure 22 (a), (b), and (c), it only makes sense to apply measures at the revealed pollution hotspots. Consequently, upon carefully inspecting the 3D geometry of the Turnhoutsebaan at the identified hotspots, 2 geometric modifications seemed attainable. The first is placing “wind catchers” on top of high buildings that are obstructing the wind flow (Figures 13 and 14). In the application of this measure, no apartments need to be demolished. The intention of the wind catchers is to direct additional air flow towards the street surface. Zhang et al. (2019) already reported that this can improve the dilution process, but these authors only studied a simplified 2D urban configuration. Thus, information on the application of this measure in a realistic 3D urban fabric is still lacking. The second is the reshaping of pitched roofs at the upwind side of the Turnhoutsebaan as flat roofs (Figures 15 and 16). This modification was chosen, because in a 3D idealized building study, pitched roofs were already found to negatively effect dilution with respect to flat roofs of the same height (Tan et al., 2019). Besides, the modification presented in Figure 15 implies an increase in the habitable space of the concerning buildings, which could be acceptable for the current residents if the building conversion were to be paid by the government.

With regard to removal by ESP, the dimensions of the used units are $L \times W \times H = (2.8 \times 0.72 \times 1.28)$ m^3 (see Section 2.5.3) and 5 units were placed at locations corresponding to parking spots. The sacrifice of 5 parking spots to implement air pollution mitigation measures seems a reasonable action. It should be noted that ESP only acts on PM.

2.5.1. Employment of wind catchers

The first mitigation measure investigated stems from the idea of modifying the local flow field in the street canyon, with the aim of enhancing the dilution process by directing additional air flow towards the street surface. It consists of wind catchers employed on top of the six tallest buildings, on the upwind side of the street canyon. A schematic of the wind catcher is shown in Figure 13. Location, visualization and dimensions of the wind catchers in the Turnhoutsebaan are shown in Figure 14.

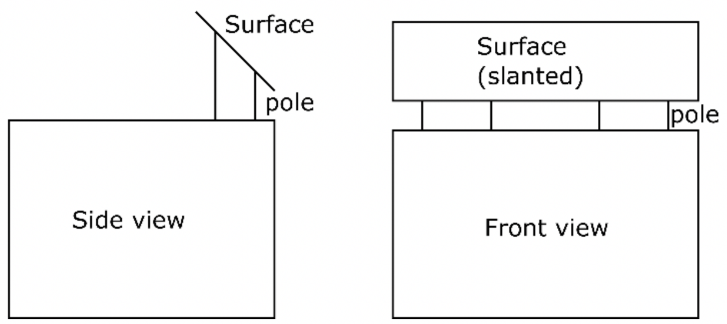

Figure 13: Schematic of the wind catcher designed for the rooftop of some strategic buildings in the Turnhoutsebaan.

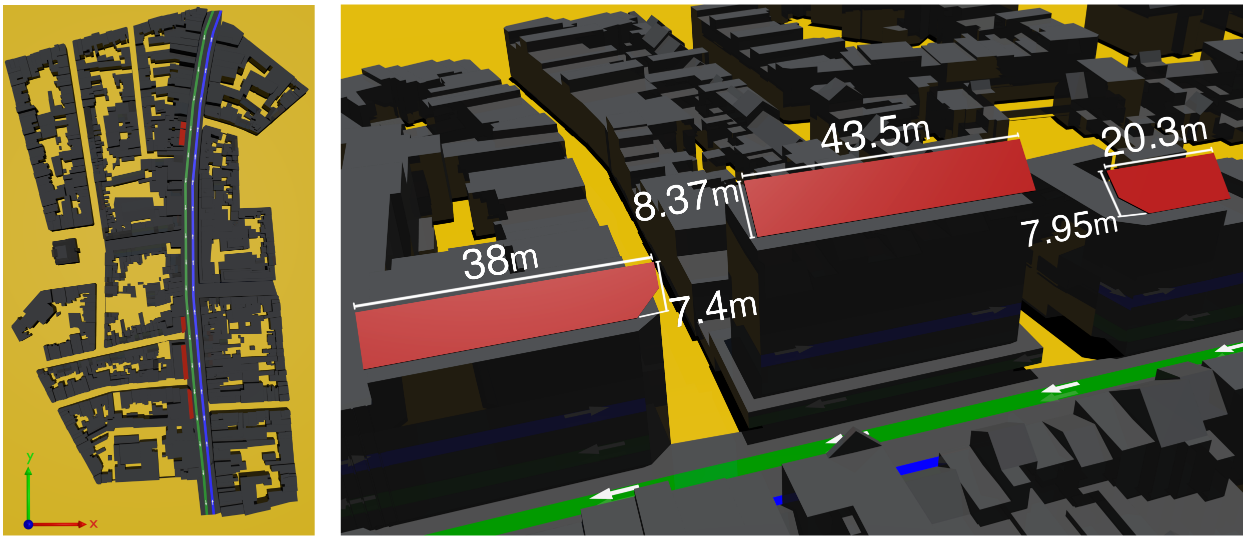

Figure 14: Location (a), visualization and dimensions (b) of the wind catchers (highlighted in red) inside the Turnhoutsebaan.

2.5.2. Targeted modification of the local geometry

The second mitigation measure, also based on the alteration of the local flow field and ventilation, consists in a targeted modification of the rooftop geometry of some buildings inside the urban canyon. In this study, two buildings with a pitched roof shape were considered suitable for this modification and converted into flat roof shaped. For this modification, two different geometric configurations were conceived and studied, as schematically displayed in Figure 15 (a) and 16 (a). In the first case, the resulting flat rooftop was set to the height of the peak of the original pitched rooftop, namely $z = 22.6$ m. In the second strategy, the converted flat rooftop was lowered to the height of the base of the pitched rooftop, namely at $z = 18.4$ m. The actual locations and modifications of the rooftop in the Turnhoutsebaan are shown in Figures 15 and 16 (b), (c), and (d).

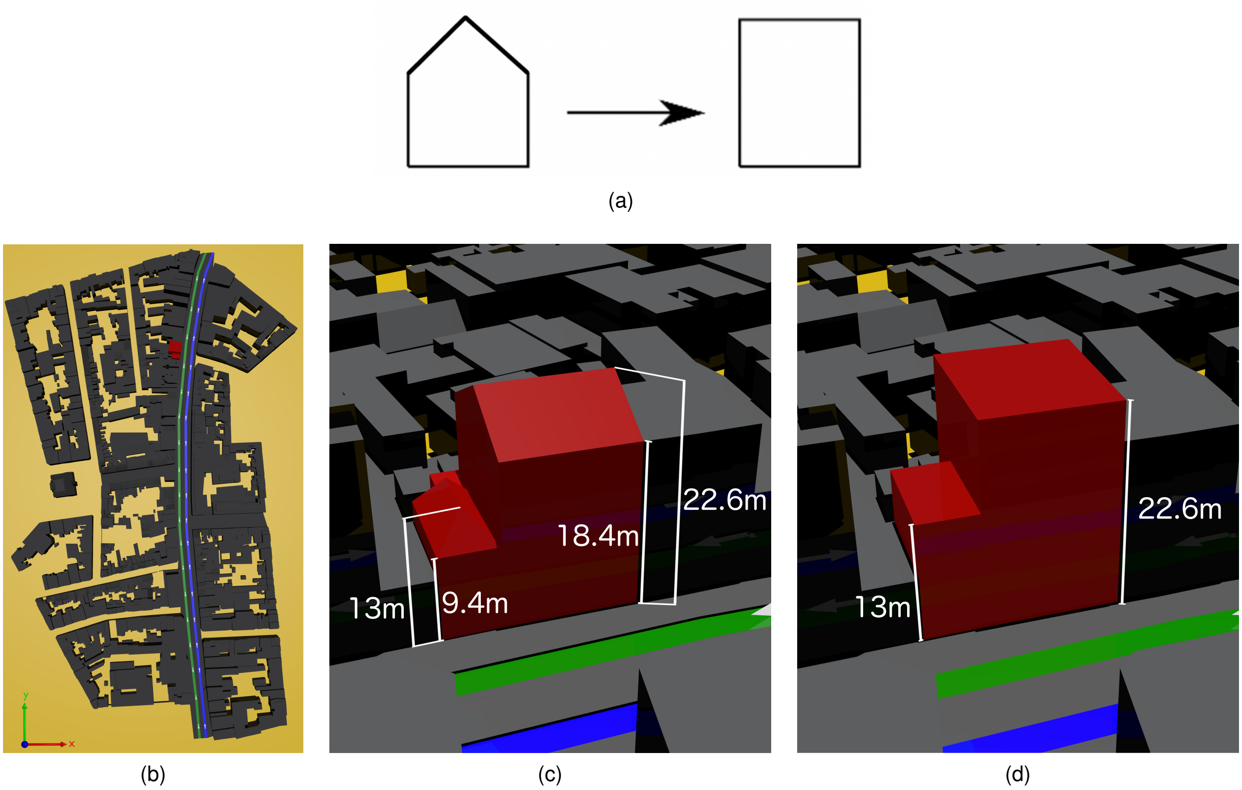

Figure 15: Schematic of the roof geometry modification based on flat rooftop elevation (a), location of the modified buildings (b), previous pitched-roof configuration (c) and applied no pitched-roof modification (d) inside the Turnhoutsebaan.

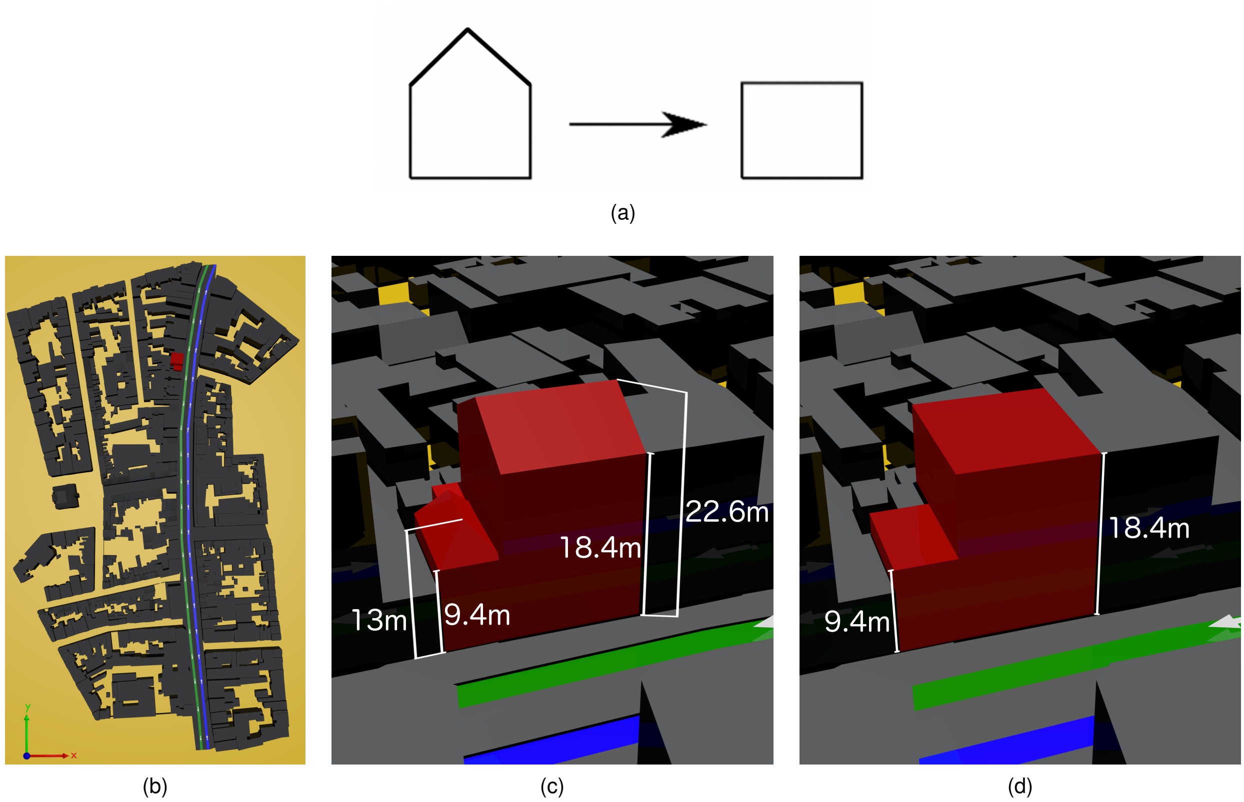

Figure 16: Schematic of the roof geometry modification based on flat rooftop lowering (a), location of the modified buildings (b), previous pitched-roof configuration (c) and applied no pitched-roof modification (d) inside the Turnhoutsebaan.

2.5.3. Employment of electrostatic precipitation (ESP)

Similarly to Blocken et al. (2016) and Vervoort et al. (2019), the third and last mitigation measure, applicable for reducing the PM_{10} concentration, consisted in the employment of commercially available ESP units. 5 ESP units were placed in strategic locations, adjacent to the street lanes at $z = 1$ m, where the pollutant tends to gather and stagnate, according to the outcomes of the simulation campaign for PM_{10}. Their location is shown in Figure 17 (a) and (b).

The ESP units (Figure 17(c)), type Aufero (ENS Clean Air Solutions, 2018), are commercially available systems with dimensions $L \times W \times H = (2.8 \times 0.72 \times 1.28)$ m^3. A maximum volumetric flow rate was assumed for each unit, namely 7500 m^3/h (or 2.552 kg/s), with a constant PM_{10} removal efficiency of 70 %, analogously to Blocken et al. (2016). The unit presents a high flexibility in orientation/configuration, both in the vertical and horizontal directions. This mitigation measure was implemented in the CFD model by explicitly depicting the 5 units (Figure 17 (a) and (b)), and setting the efficiency and the total inflow/outflow of both air and PM_{10} according to the ideal, aforementioned specifications via a user-defined function.

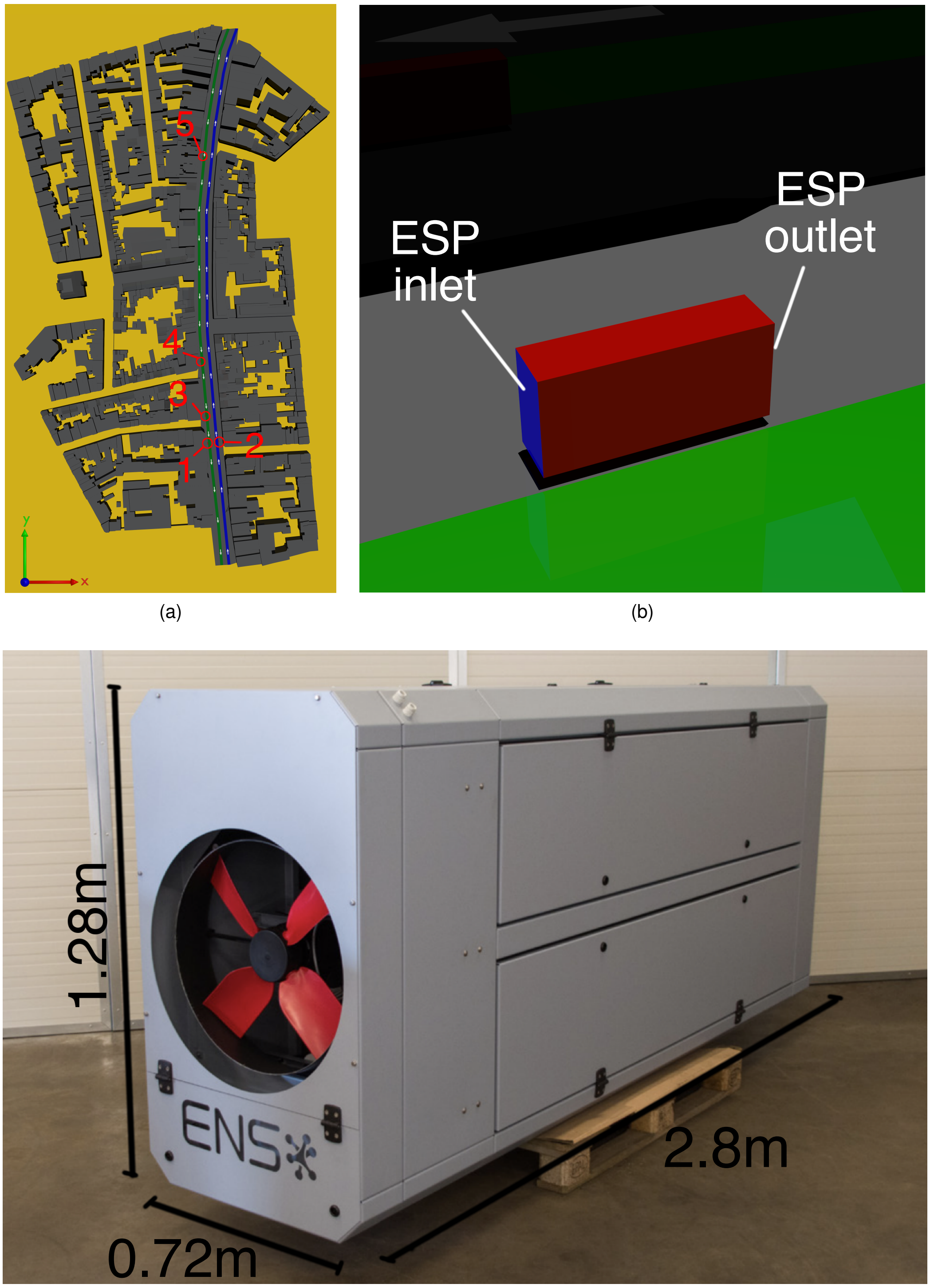

Figure 17: Schematic of the locations of the 5 electrostatic precipitation (ESP) units inside the domain (a), zoom and orientation of the 5th unit (b) and view of the ESP unit (c) (ENS Clean Air Solutions, 2018).

3. Results and discussion

Figure 18 shows the comparison of experimental data and numerical prediction of wind directions and xy velocity magnitudes at the 6 considered locations inside the urban canyon. The turbulence model employed is the ABL approach from Section 2.1, with hybrid BIA (Longo et al., 2020b) and the NLEV model by Ehrhard and Moussiopoulos (2000) applied inside the BIA. From Figure 18, it can be noticed that the velocity directions were narrowly represented by the ABL turbulence model, at all the locations considered. An accurate prediction was also reached for the xy velocity magnitude, with the highest discrepancy witnessed at location 4, where the ABL model tends to overpredict the velocity field. However, the velocity measurements in the street were performed during less favorable conditions than the wind directions (Section 2.2.5). To improve the model validation in the future, it is proposed to model combinations of several wind directions and speeds, while also performing a longer measurement campaign. In this way it will be very likely, that the model can be validated with data where sufficiently long periods occur with conditions very close to inflow conditions used in the model.

Figure 19 (a) and (b) show the contour plots of velocity magnitude in the vertical symmetry $y = 0$ m and the horizontal $z = 1.43$ m planes. From Figure 19 (a) it is possible to observe the distribution of the velocity field in the vertical plane and the homogeneity of velocity upwind and downwind the depicted district. The upwind homogeneity is required when performing simulations of buildings immersed in an ABL flow (Franke et al., 2007), but it is well known that achieving it is problematic (Blocken et al., 2007; Moonen et al., 2012). This clearly highlights an important advantage of the employed ABL modeling methodology (being in accordance with the observations in Section 2.3). Besides, in the urban area, extended low speed and recirculation zones are bent around and downwind the buildings, and inside the main urban canyon. The contour plot at the horizontal plane (Figure 19 (b)) further shows that the velocity field is strongly heterogeneous inside the urban canyon. The canyon can be divided in two types of areas, where one type is characterized by a more intense ventilation and the other is showing stagnation phenomena. These stagnating areas can potentially lead to higher concentrations of pollutants, due to the low dilution process involved.

Figure 20 shows the contour plots of the BIA at the vertical $y = 0$ m and horizontal $z = 1.43$ m planes. A blue color represents a deviation from the undisturbed flow field equal to 0, while a red color (deviation equal to 1) is indicative of a fully disturbed flow field. It can be noticed that all the buildings of the considered district are correctly detected and completely enveloped by the BIA, where NLEV models are employed.

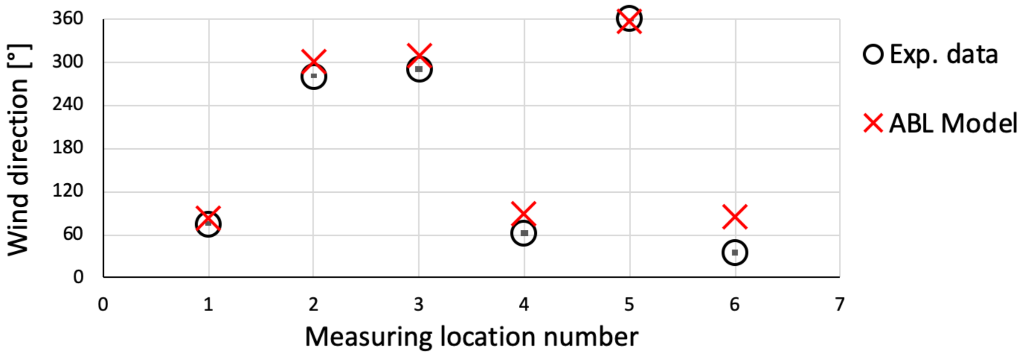

(a)

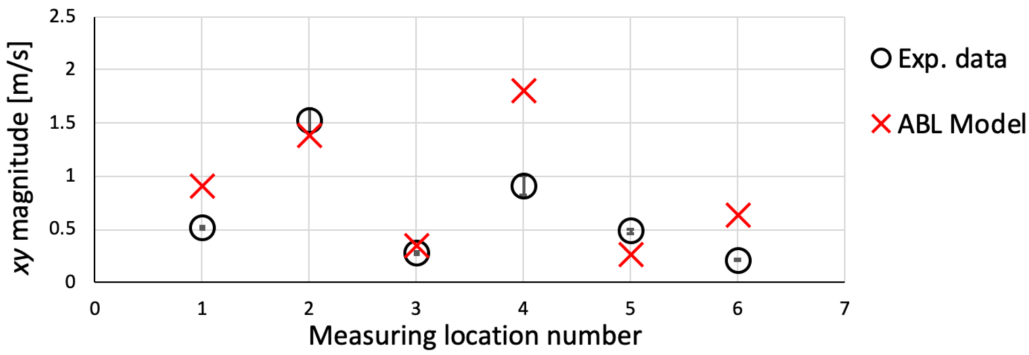

(b)

Figure 18: Comparison of experimental data and numerical prediction of wind direction (a) and xy velocity magnitude (b) for the Antwerp test case, in the locations shown in Figure 6. The experimental data is displayed in black circles (the error bars represent the standard error of the mean) while the numerical predictions of the ABL model are represented by red crosses.

Figure 21 shows a comparison of experimental data and modeled concentration, in terms of difference between total concentration and background concentration. Error propagation was performed on the results for the variable Sc_t configuration (red crosses), stemming from the uncertainty of the background and the measured concentrations. In addition, the configurations based on the ABL turbulence model with $Sc_t = 0.3$ and $Sc_t = 0.7$ were tested. The most balanced and accurate prediction is shown by the variable Sc_t formulation, with the highest discrepancies witnessed at location 3. Among the constant Sc_t numbers, the configuration with $Sc_t = 0.3$ shows a good agreement with the experimental data. Its trend is that of underestimating the concentration field close to the upwind facade (locations 1-3-5) and slightly overpredicting it nearby the downwind facades (locations 2-3). The trend of the $Sc_t = 0.7$ is that of overestimating the concentration field at all the considered locations. As a remark, it should be emphasized that there is still room for improvement in the accuracy of the measurement of the background concentration during the measurement campaign (Section 2.2.6). In the future, measuring the concentration flowing into the zone of interest with the wind and simultaneously measuring the concentration in the zone of interest, will further

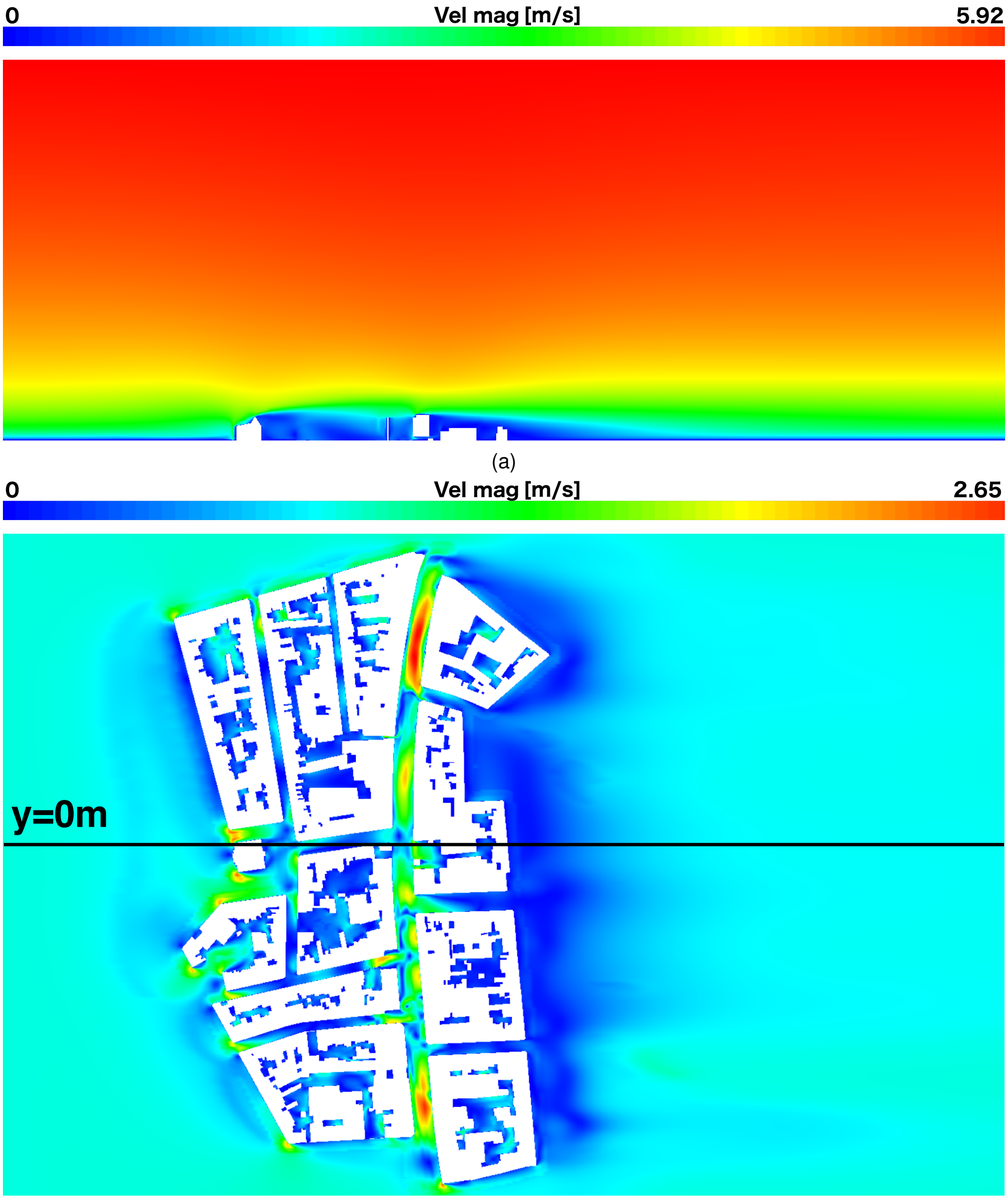

(a)

(b)

Figure 19: Contour plots of velocity magnitude at the vertical $y = 0$ m (a) and Horizontal $z = 1.43$ m (b) planes for the Antwerp test case.

improve the confidence in the conclusions that can be drawn from the measurement campaign results.

Figure 22 shows the horizontal distribution of the NO_2 concentration, at six different heights: $z = 1$ m, $z = 1.43$ m, $z = 2$ m, $z = 5$ m, $z = 10$ m and $z = 20$ m. From these contours, it can be noticed that, as expected, the pollutant distribution inside an urban canyon or, more in general, in an urban context, can be very heterogeneous. In this regard, some specific areas, where the pollutant is stagnating and is less diluted, can be easily located. When comparing and Figure 19 (b) Figure 22 (a), it is clear that the high concentration areas correspond narrowly to the low velocity areas. These low velocity areas occur mainly at places where high buildings are placed at the upwind side of the Turnhoutsebaan (Figures 11 (b) and 14 (a) and (b)). Hence, the negative effect of the upwind high buildings on the ventilation capacity can be identified as the main cause of the pollution hotspots. Moreover, it is further demonstrated that, also in a real-scale street canyon framework, the concentration field strongly depends on the z coordinate, with a lowering of the pollutant level as the vertical distance from the ground increases and, consequently, as the air entrainment tends to rise. This is especially evident when considering the heights $z = 5$ m, $z = 10$ m and $z = 20$ m, where in correspondence of the emitting street the peaks of concentrations are strongly damped and reduced, approaching the values of the background concentration. Besides, comparing the NO_2 results to the VMM pollution measurement station (Figure 4) data further increases the trustworthiness of the modeled concentration results. From this data, in Section 2.2.4, the background concentration and increased concentration due to traffic emissions nearby the road of NO_2 were estimated, which are 35.54 and 62.47 µg/m^3 respectively. The former was estimated from data from station R801 and was also used as background concentration in the model. The latter was estimated from data from station R802 and corresponds to the model results, which can be seen in Figure 22 (a), (b), and (c). At many locations that do not lie within the identified hotspots (i.e. where the remedation measures were applied, Figure 14 (a)), where increased NO_2 concentrations occur (upwind side of the Turnhoutsebaan, left side in Figure 22) and which are similar to the location of measurement station R802 with respect to the traffic lane (boundary buildings-street), the NO_2 concentration is indeed close to 62.47 µg/m^3. NO_2 concentration values extracted from the model at said locations at a height of 3.5 m range from 40 to 54 µg/m^3.

The behavior of the employed Sc_t can be appreciated in Figure 23, highlighting the local variability of the approach adopted. The turbulent Schmidt number varies within the suggested values in ABL literature, from a minimum of 0.2 to a maximum of 0.85. Apart from the molecular Schmidt, its local variability is directly related to the local turbulence level, depending on the turbulent Reynolds number, the strain-rate and vorticity invaritants.

Based on the outcomes obtained at this stage, i.e. the distribution of pollutant concentration and the detection of pollutant stagnation zones, in the following section, three pollutant remediation measures were conceived, employed and their outcomes finally analyzed.

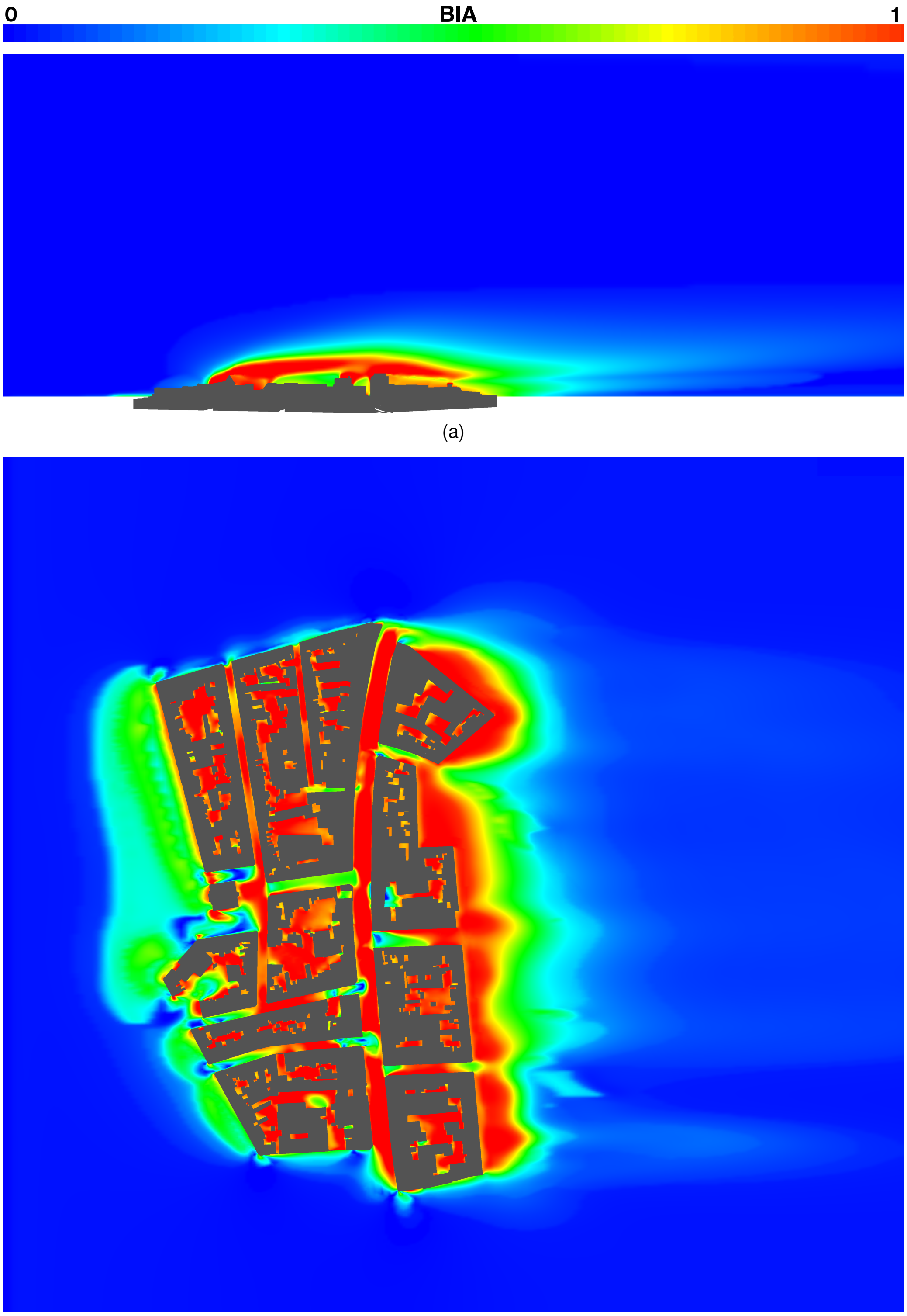

(a)

(b)

Figure 20: Contour plots of building influence area (BIA) at the vertical $y = 0$ m (a) and Horizontal $z = 1.43$ m (b) planes for the Antwerp test case.

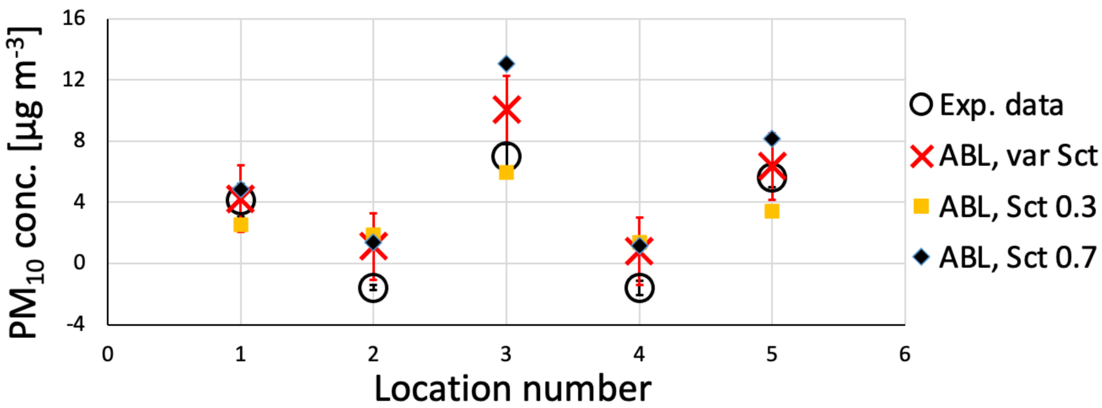

Figure 21: Comparison of experimental data and numerical predictions of PM_{10} concentration, in terms of difference between total concentration and background concentration, for the Antwerp test case, in the locations shown in Figure 6. The experimental data is displayed in black circles (error stemming from standard errors of the mean of the background concentration and the measured concentration), the numerical predictions of the ABL model with the variable Sc_t formulation are represented by red crosses (errors stemming from the standard error of the mean of the background concentration used in the model), the predictions obtained with $Sc_t = 0.3$ are displayed in yellow squares and those with $Sc_t = 0.7$ in black rhombus.

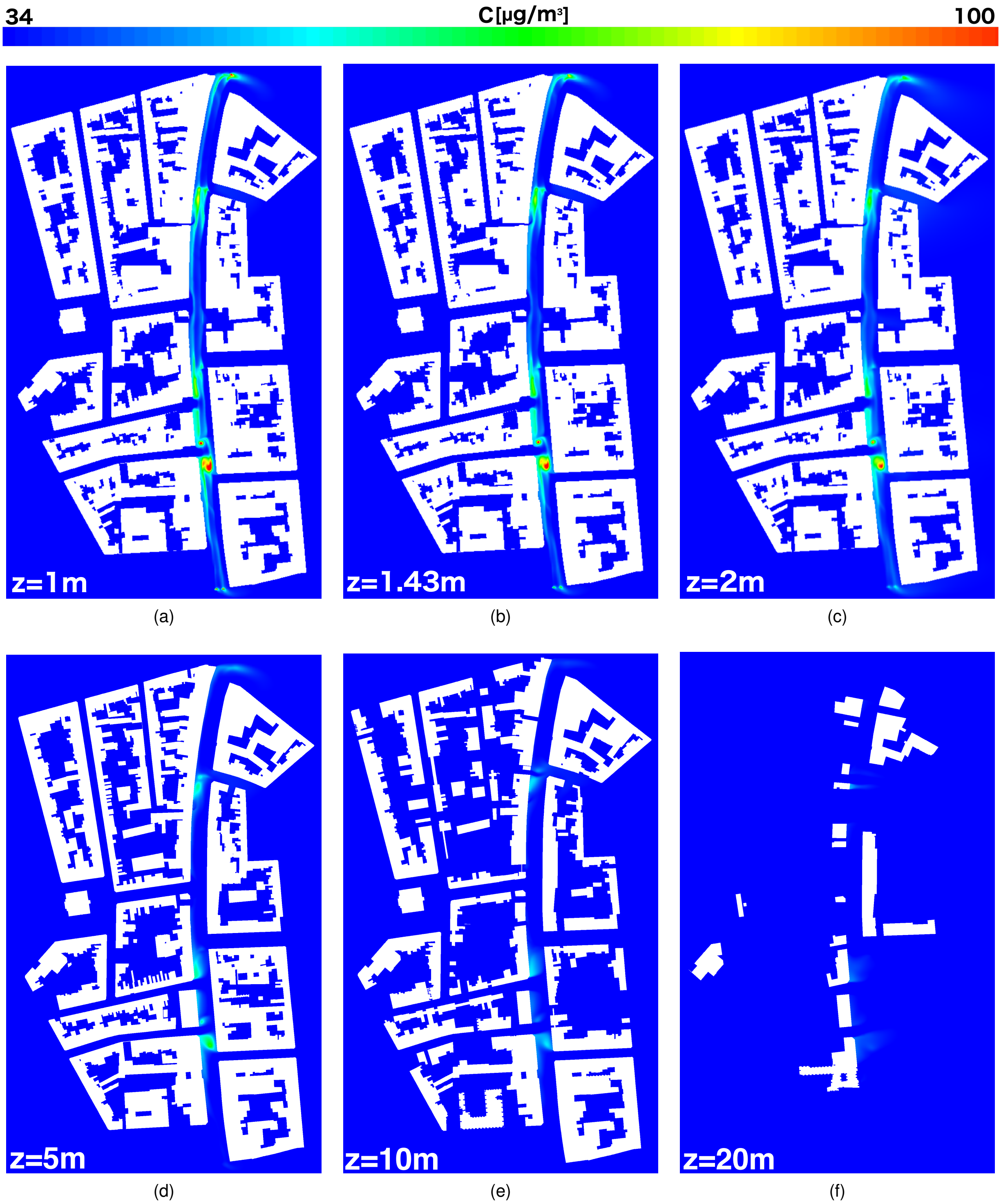

Figure 22: Horizontal contour plots of NO_2 concentration at the planes $z = 1$ m (a), $z = 1.43$ m (b) and $z = 2$ m (c), $z = 5$ m (d), $z = 10$ m (e) and $z = 20$ m (f) of the Turnhoutsebaan, clipped between 34 μg/m^3 and 100 μg/m^3.

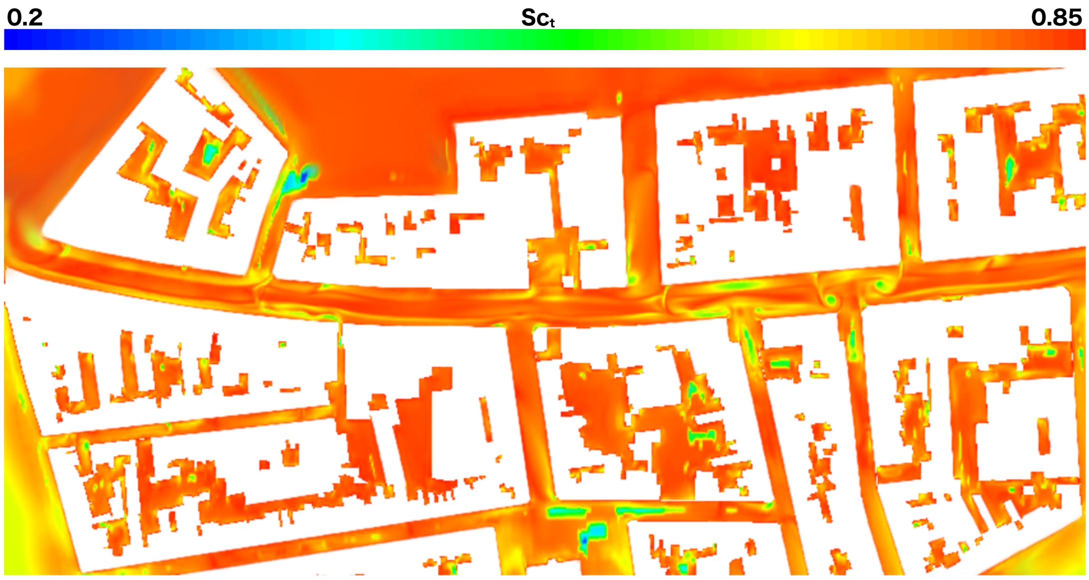

Figure 23: Horizontal contour plots of variable turbulent Schmidt number, Sc_t, in the horizontal $z = 1.43$ m plane for the Antwerp test case.

3.1. Investigated mitigation measures

Once the pollutant distribution inside the urban canyon for one of the most relevant wind directions has been determined, the next step is to propose feasible and efficient mitigation measures, especially in relation to the existing orography.

3.1.1. Employment of wind catchers

The effect of the wind catcher, shown in the contour plots in Figure 24 at the horizontal $z = 2$ m plane, is that of modifying the air entrainment in the street canyon, resulting in a more efficient dilution process. A reduction of pollutant concentration can be observed, improving the local breathability inside the urban canyon (in the locations close to the wind catchers) and lowering the local peaks of concentrations (Figure 24). A similar reduction was observed when considering other horizontal planes, at $z = 1$ m, $z = 1.43$ m. The most remarkable differences are witnessed at the pedestrian level, reaching, in some specific areas, where pollutant tended to gather and stagnate, a concentration reduction up to 37 %. The same considerations can be done considering Figure 25, where the percentage of pollutant reduction is displayed.

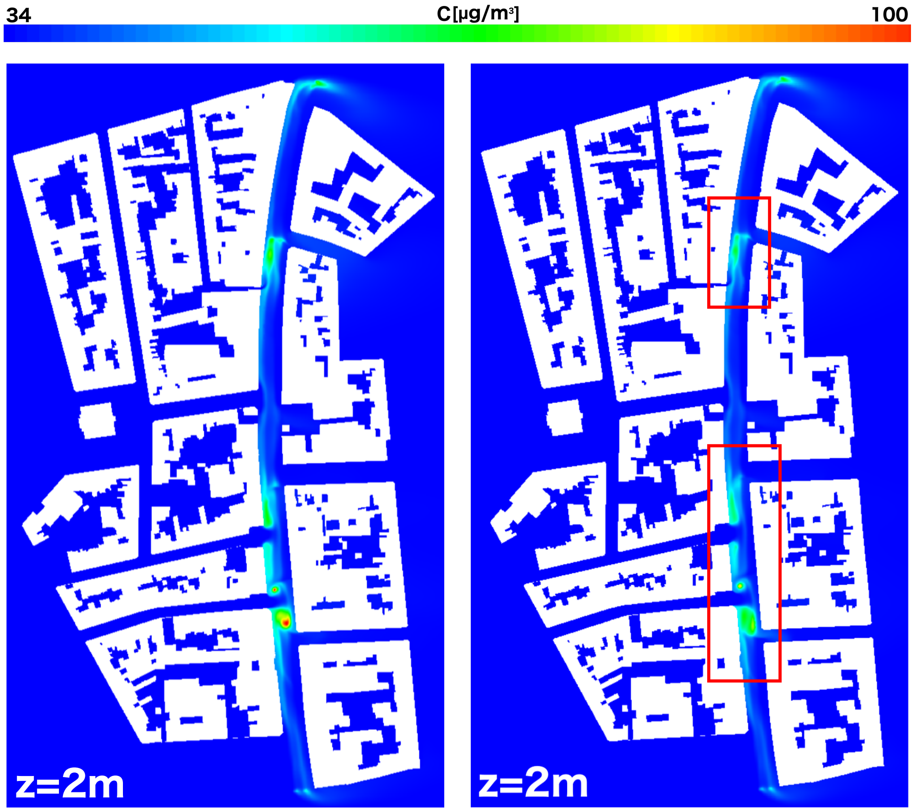

(a) Base configuration

(b) Configuration with wind catchers

Figure 24: Comparison of NO_2 concentration for the base case and the one displaying the wind catchers. The red rectangles envelope the areas interested by the employed wind catchers.

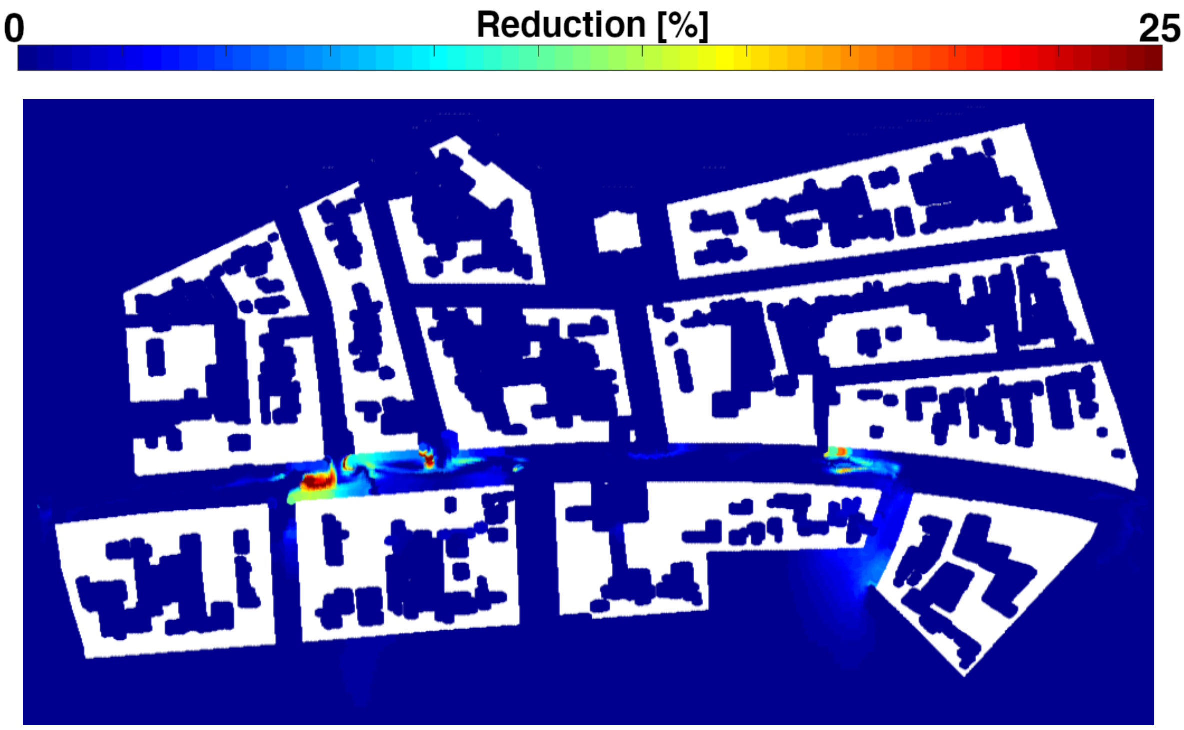

Figure 25: Reduction in percentage of NO_2 concentration due to the application of wind catchers with respect to the base case, at a height of 2 m. The values are clipped between 0 and 25.

3.1.2. Targeted modification of the local rooftop

For the first geometric modification (Figure 15), a minor effect on local pollutant level can be witnessed. From the contour plots in Figure 26, it is possible to notice a limited reduction of pollution, around 2-3 % in the locations close to the ground level. An analogous trend was witnessed for a wide range of horizontal planes, with a height 0 m $< z < 4$ m. Moreover, this effect was limited just to the areas in the proximity of the modified buildings. It should however be noted that the rooftop modifications are placed at the border of and even partly beside the pollution hotspot, (Figures 15 (a) and 26 (a)) which is far from optimal. (No pitched roof were present at the center of any of the concentration hotspots.)

As for the second rooftop modification (Figure 16), analogous conclusions can be drawn. Again, only a

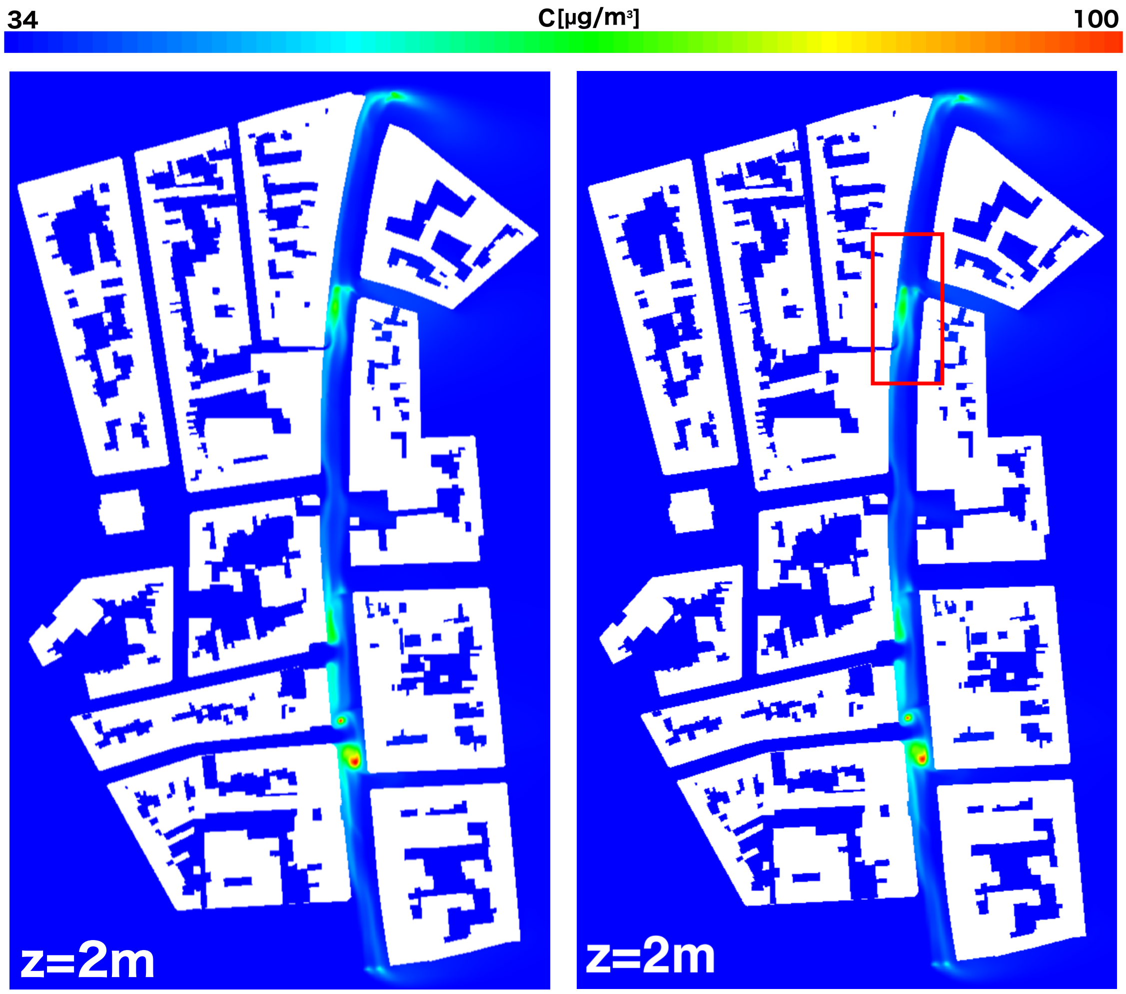

(a) Base configuration

(b) Configuration with no pitched roof buildings

Figure 26: Comparison of NO_2 concentration for the base case and the one displaying the modified rooftop from Figure 15. The red rectangle envelopes the area interested by the proposed rooftop modification.

limited variation in the pollutant concentration can be witnessed in the area of interest, with minor deviations with respect to the previous rooftop modification (Figure 27). This trend was observed for all horizontal planes in the range 0 m $< z < 4$ m. Moreover, surface and volume averaged concentration reports further confirmed this observation.

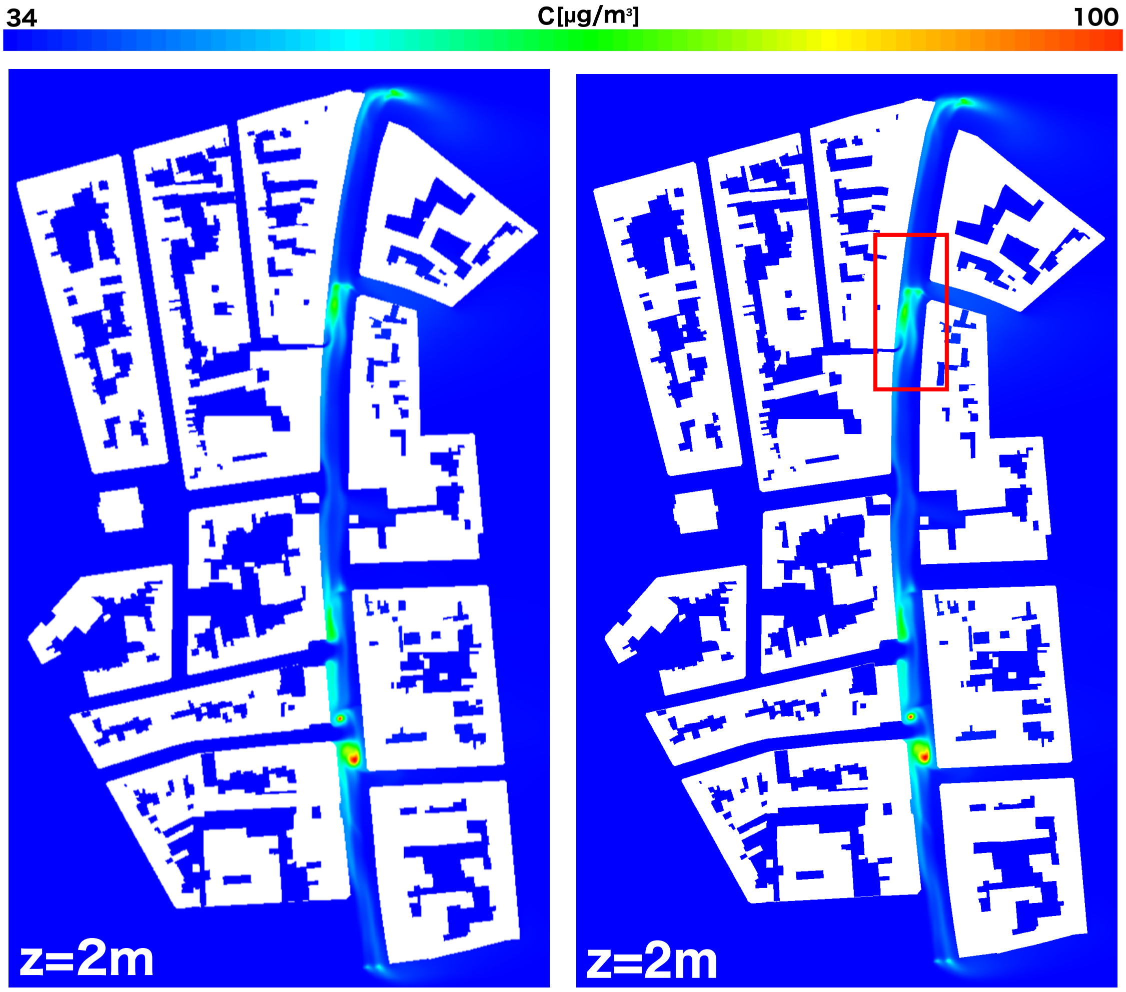

(a) Base configuration

(b) Configuration with no pitched roof

Figure 27: Comparison of NO_2 concentration for the base case and the one displaying the modified rooftop from Figure 16. The red rectangle envelopes the area interested by the proposed rooftop modification.

Since the rooftop modifications were not optimally placed, a more thorough analysis could still reveal whether the measure has potential. To visualize the effect of the rooftop modification on the velocity field, Figure 28 shows the comparison of velocity magnitude and direction between the base case and the two configurations under study, at the location of the modified rooftop ($y = 168$ m). A large clockwise vortex is present inside the canyon for the three configurations under study with the lowest velocities in the central locations of the canyon. No major differences can be spotted between the three configurations in the canyon. However, the first modification (namely the conversion of pitched to flat roofs from Figure 15), results in slight increase of the velocity at the top of the street canyon. This could result in improved removal of pollutants. As for the second rooftop modification (namely the lowering of the rooftop from Figure 16), it leads to a slightly reduced recirculation area, especially at the highest locations of the vortex (16 m $< z < 23$ m). This is interpreted as an effect related to the reduction in height of the upwind building, resulting in a lower blockage of the undisturbed flow field.

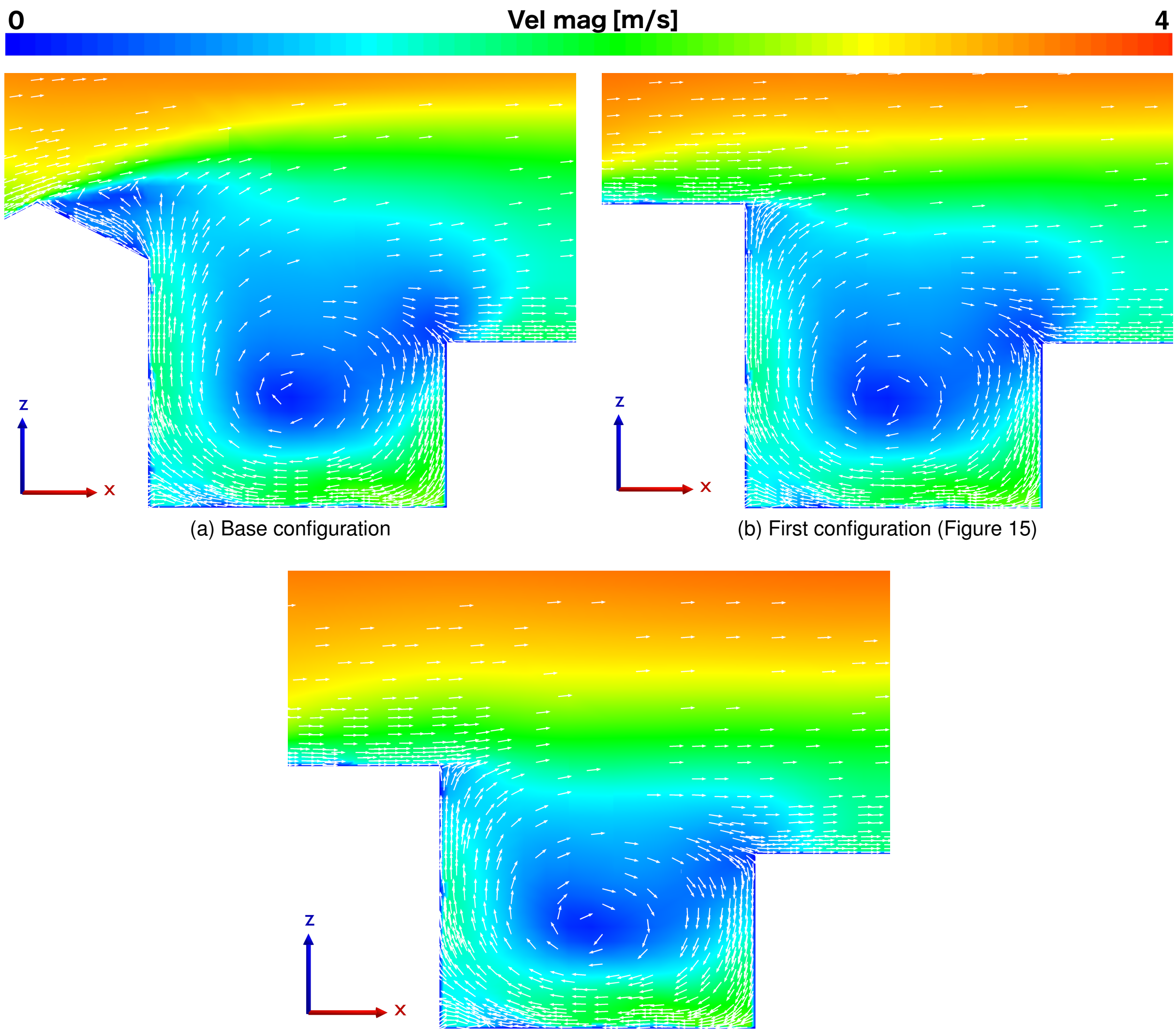

(a) Base configuration

(b) First configuration (Figure 15)

(c) Second no-pitched roof configuration (Figure 16)

Figure 28: Comparison of velocity magnitude and direction between the base case and the two rooftop configurations under study, in the vertical plane $y = 168$ m cutting the main roof from Figure 15 and 16. The velocity is clipped to a maximum value of 4 m/s.

In conclusion, the rooftop modifications were not very effective. It should however be noted that, unlike the wind catchers solution, in the present strategy only a limited number of buildings were feasible for the proposed geometric modification. Consequently, a more reduced area was actually affected by the geometric modification. This modification was, furthermore, applicable only in proximity of an area where there are no peaks of pollutant concentration. In any case, these results indicate that further studying the effect of pitched roofs in traffic intensive streets in realistic case studies, can help shape building regulations for the cleaner cities of the future.

3.1.3. Employment of electrostatic precipitation (ESP)

The concentration contour plots of Figure 29, at three different horizontal planes ($z = 1$ m, $z = 1.43$ m and $z = 2$ m), with and without ESP units, already indicate that the concentration level, in an extended area around each single unit, is strongly reduced by the remedial action of ESP. Zoomed Figure 32 shows a clear view of this, as does Figure 30, which shows the pollutant reduction in percentages. As one would expect, the ESP devices are able to efficaciously impact the concentration field in a larger area, with respect to the first two mitigation measures. This is also related to the fact that this strategy is based on the direct reduction of the pollutant level, and not just on the enhancement of the local dilution process. In particular, in the area around the ESP unit 1, 2 and 3, the peaks of concentration of PM_{10} are damped and strongly reduced. This is particularly interesting, because applying the ESPs lowers the concentrations at the locations of the peaks almost entirely below the EU one day average limit value for PM_{10} of 50 µg/m3 (not to be exceeded more than 35 times a calendar year) EU (2015). Since the CFD model does not deliver one day average results, it is not certain that this results in attaining the EU legislation or whether these locations were problematic in the first place. However, the simulated weather conditions are one of the most frequently occurring (Section 2.2.2). Therefore, in reality, the ESPs will be able to lower the concentrations substantially for large periods in time. This clearly indicates that ESP can be a very interesting measure at problematic places in relation to air quality legislation.

In Figures 31, 32 and 33 it is possible to analyze the effect that the presence of the ESP units has on the velocity and concentration fields, in the area close to the precipitators 1, 2, 3. In this location, characterized by low velocities and where the pollutant is stagnating, the ESP units are capable to strongly reduce (up to 40 %) the concentration level. From Figure 32, it can be noticed that, the concentration stagnation zones are strongly reduced in size and intensity. This is confirmed also by the concentration comparison in Figure 33 and further suggests that the employment of ESP units in strategic locations can lead to a relevant improvement in the local breathability level. Surface and volume averaged reports further confirmed the observations.

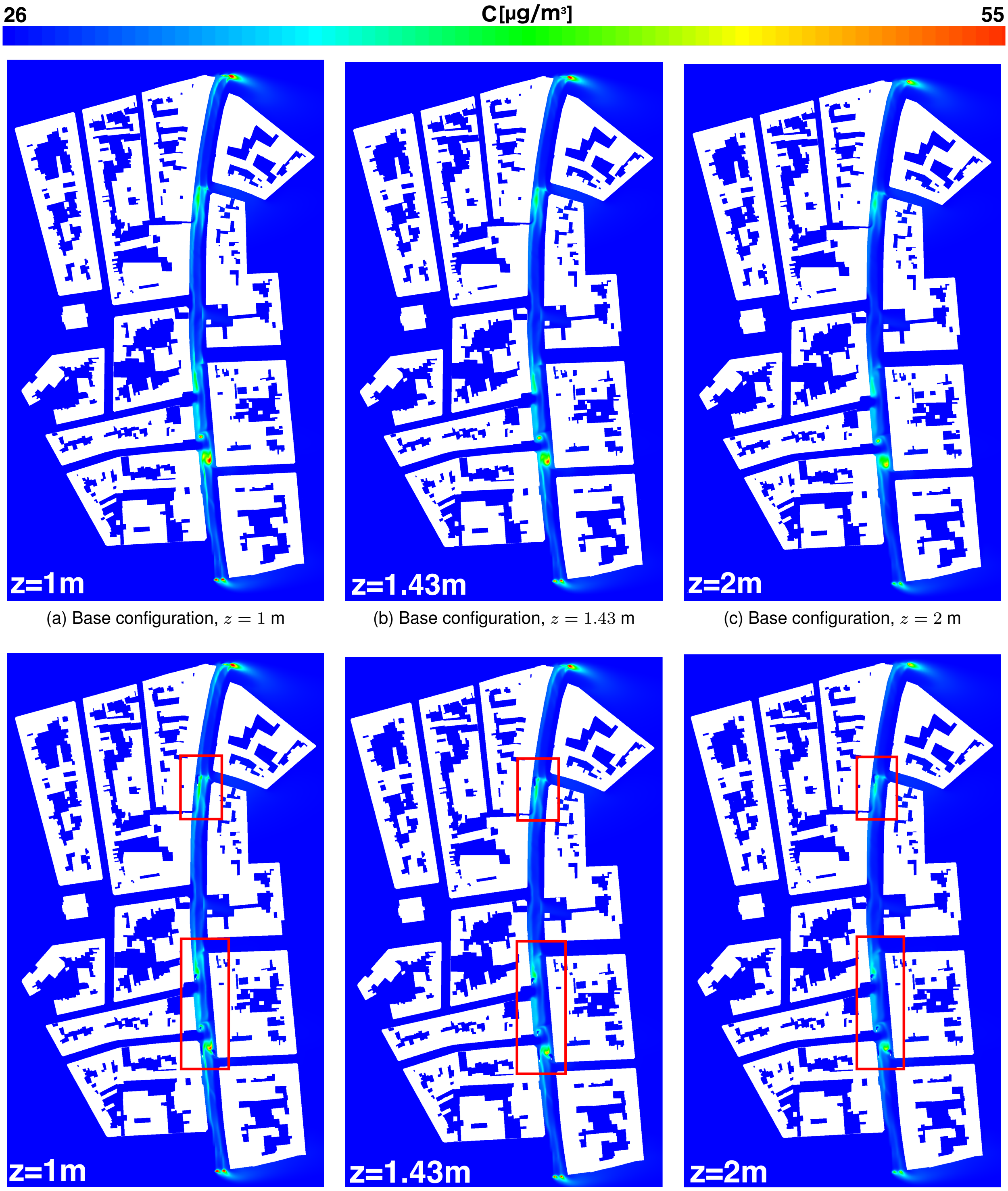

(a) Base configuration, $z = 1$ m

(b) Base configuration, $z = 1.43$ m

(c) Base configuration, $z = 2$ m

(d) ESP configuration, $z = 1$ m

(e) ESP configuration, $z = 1.43$ m

(f) ESP configuration, $z = 2$ m

Figure 29: Comparison of PM_{10} concentration for the base case and the case with the presence of the ESP devices from Figure 17. The red rectangles envelope the areas interested by the action of the ESP units.

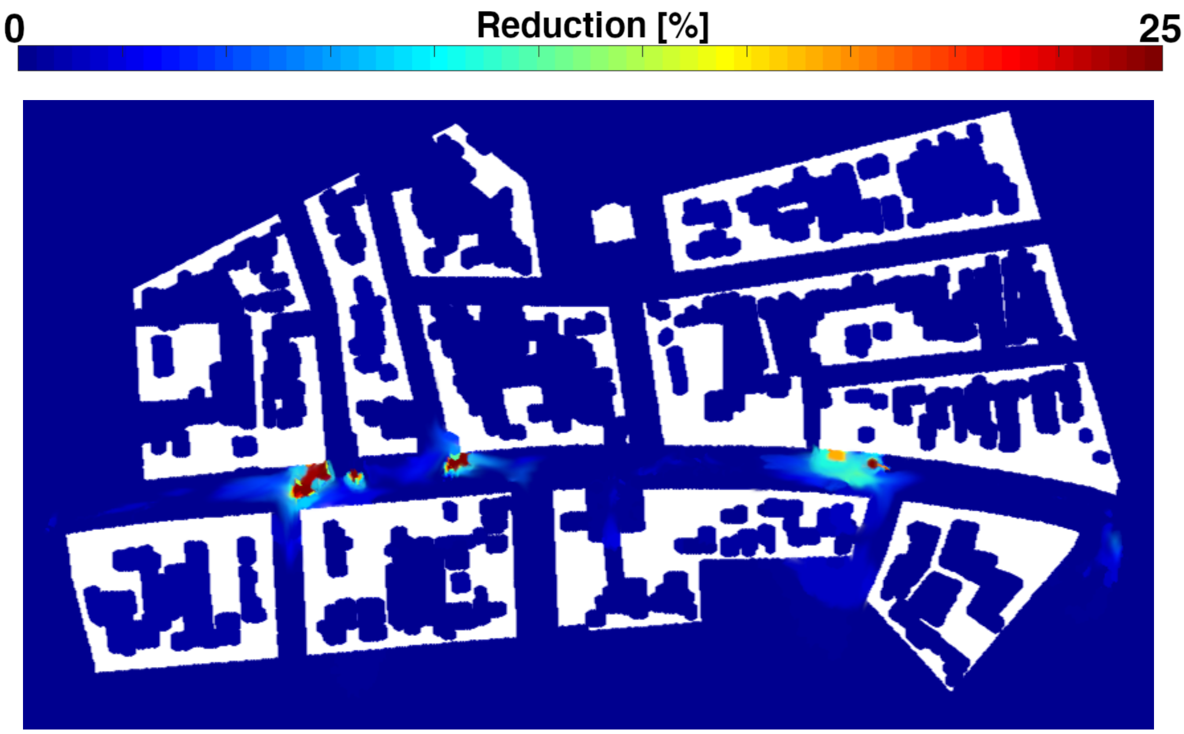

Figure 30: Reduction in percentage of PM_{10} concentration due to the application of ESP units with respect to the base case, at a height of 2 m. The values are clipped between 0 and 25.

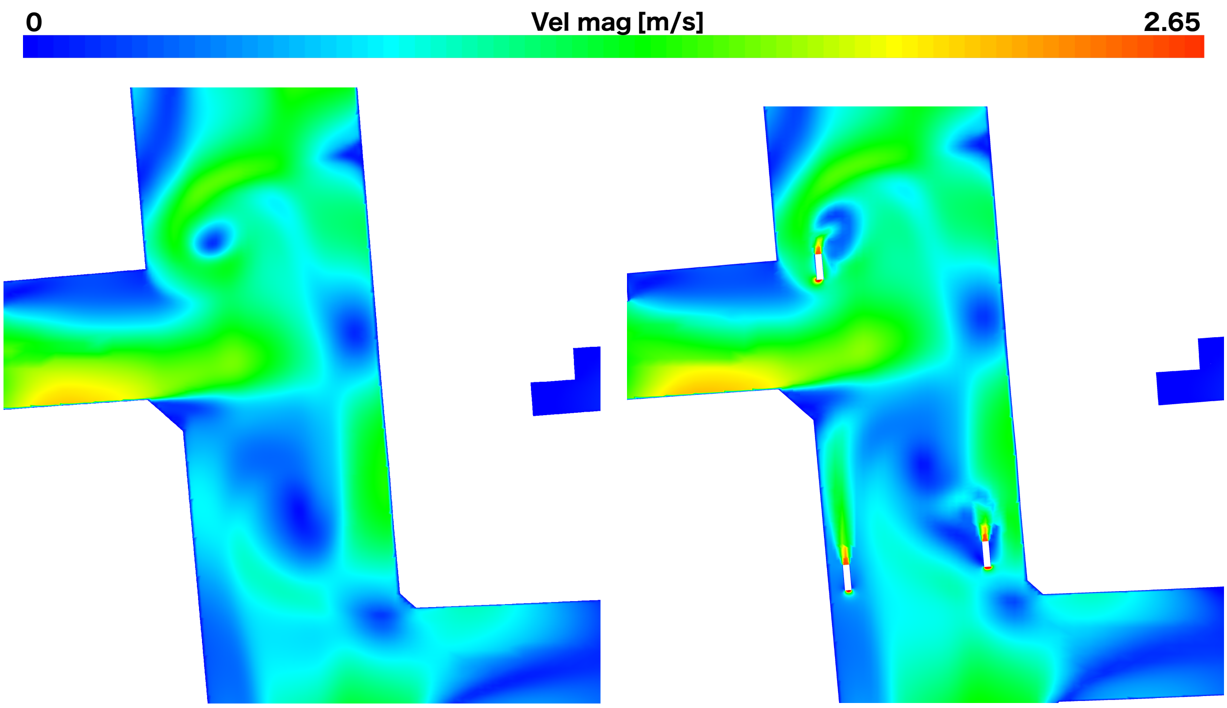

(a) Base case.

(b) Case with ESP.

Figure 31: Contour plots of velocity magnitude at the horizontal $z = 1.43$ m plane, in a zoomed area of the Turnhoutsebaan, for the base case configuration (a) and the one including the ESP units 1, 2 and 3 (b).

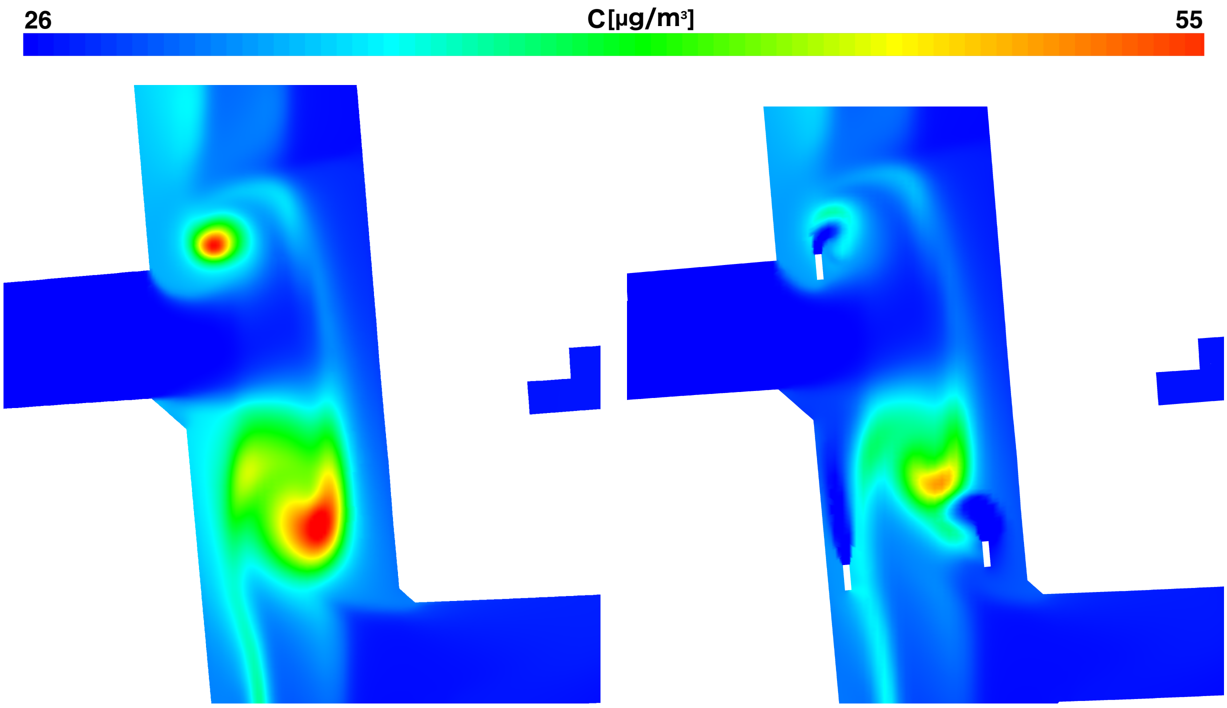

(a) Base case.

(b) Case with ESP.

Figure 32: Contour plots of PM_{10} concentration at the horizontal $z = 1.43$ m plane, in a zoomed area of the Turnhoutsebaan, for the base case configuration (a) and the one including the ESP units 1,2 and 3 (b).

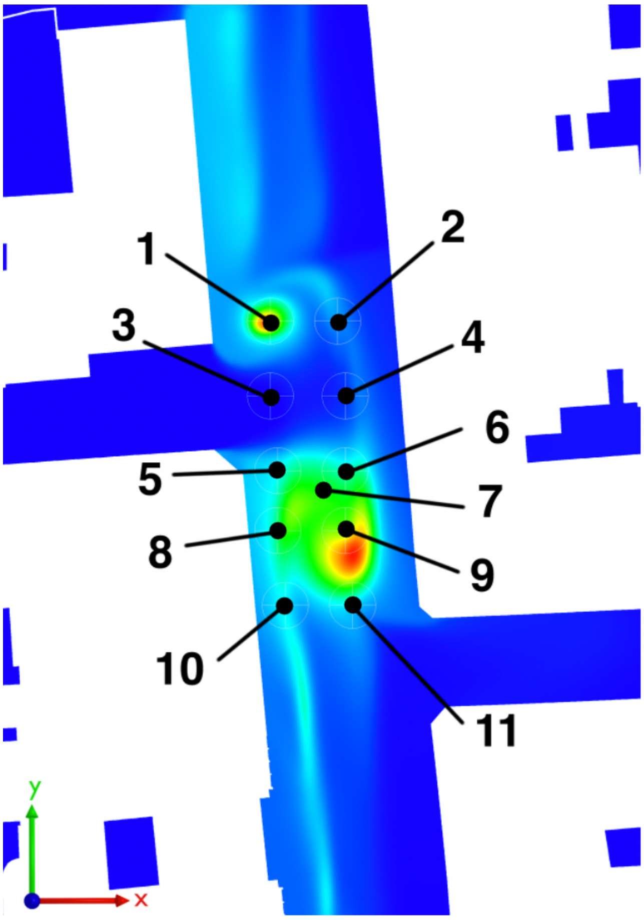

No.	x(m)	y(m)	z(m)
1	5.00	-172.00	1.43
2	14.00	-172.00	1.43
3	5.00	-182.00	1.43
4	15.00	-182.00	1.43
5	6.00	-192.00	1.43
6	15.00	-192.00	1.43
7	12.01	-195.00	1.42
8	6.00	-200.00	1.43
9	15.00	-200.00	1.43
10	7.00	-210.00	1.43
11	16.00	-210.00	1.43

(a) Selected locations for comparison

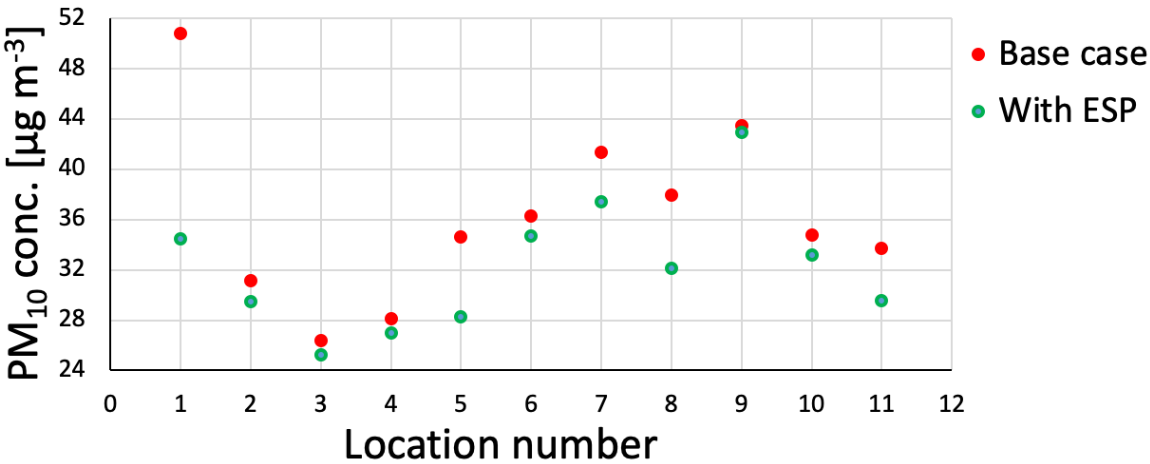

(b) Comparison between base and ESP cases

Figure 33: Comparison at 11 selected locations of PM_{10} concentration between the base case (red dots) and the one provided with ESP (green dot).

4. Summary and conclusion

Urban air pollution is a serious environmental issue and several of the involved air pollutants - such as PM, NO_x, and O_3 - are severely affecting human health. The relevance of traffic emissions of NO_x and PM was identified. Consequently, studying traffic emissions in urban environments both for NO_x and PM remains a meaningful task. In recent times, decreases in PM and NO_x concentrations were observed in some areas, e.g. Europe. However, sixteen countries of the EU still registered NO_2 concentrations exceeding the annual prefixed limit value. Moreover, the spatial density of pollution measurement stations in Europe is limited, while additional measurement campaigns indicate that large concentration differences occur at small spatial scales. This urges for a more detailed investigation of urban air pollution. Besides, the occurrence of large concentration differences also indicates that applying local air pollution remediation measures at pollution hotspots might be a good idea. Two potentially interesting measures were identified, air pollutant removal by ESP and altering the urban geometry to enhance natural ventilation and dilution of pollutants. Research on the application of these measures in a realistic urban street was lacking. As a results of these literature findings, the main goals of this study were formulated:

- to search for relevant traffic-related air pollutant concentration patterns on detailed spatial scales in an urban street, by CFD modeling of NO_2 and PM_{10} traffic emissions;
- to test and analyze the behavior of an advanced ABL turbulence and dispersion model in a realistic and complex urban street;
- to conceptualize and employ different realistic and feasible mitigation measures that can be applied locally at pollution hotspots;
- to detect which of the proposed strategies act as the most performing remediation measure.

To attain these goals, an extended traffic area of Antwerp was explicitly depicted and the dispersion phenomena related to vehicular traffic were studied in detail through CFD. Two main traffic-related pollutants were analyzed: NO_2 and PM_{10}. After a validation over a wind tunnel scaled canyon, a turbulence model specific for ABL coupled to a variable Sc_t formulation was employed for the Antwerp test case, further validating both the velocity and the concentration fields with experimental data. Finally, three local remediation measures were simulated and analyzed.

Focusing on the findings, the pollutant concentration level inside the street is strongly heterogeneous, closely depending on the local flow field and, consequently, on the urban orography. In this regard, several pollution hotspots were identified in the street, at locations where high buildings are restricting the natural ventilation. To improve the breathability at these hotspots, three remediation measures were conceptualized and studied: employment of wind catchers, targeted rooftop modification, and employment of ESP devices. Differently from previous studies, the remediation measures were applied on a realistic 3D test case, taking into account the local urban configuration and the feasibility of the proposed strategies. Results show that the greatest pollutant reduction is guaranteed by the employment of wind catchers (concentration reduction up to 37 %) and, especially, ESP (concentration reduction up to 40 %). Additional advantages of the wind catchers are that they work on all pollutants and that they do not entail an operational cost. An additional advantage of the ESP, is its higher feasibility as compared to the wind catchers. As for the rooftop modification, the following should be noted. Taking into account the concentration pattern and the urban topography, it was impossible to optimally place this measure at the center of a pollution hotspot. Optimal placement, or application to a larger number of buildings could lead to a more efficient pollutant reduction.

Besides, it was demonstrated that the application of the proposed remediation strategies requires that first a detailed CFD study is performed, in order to locate the stagnation areas and, consequently, the key locations where it is appropriate to act. This is true also for the ESP measures, whose employment and placing is characterized by an increased degree of freedom with respect to the two previous strategies. This further demonstrates the value of CFD studies in mitigating urban air pollution.

With regard to the used advanced ABL turbulence and disperion model, firstly, the validation over the wind tunnel scaled canyon already demonstrated that the variable Sc_t formulation can improve the reliability of near-field building dispersion modeling. Secondly, also in the realistic urban street, the ABL methodology showed accurate performance. The velocity magnitude, velocity direction, and PM_{10} concentration showed a good agreement with the field measurements. Besides, the following matters were demonstrated. The inflowing velocity profiles displayed horizontal homogeneity. The BIA concept, which allows to automatically switch to suitable turbulence modeling around buildings, was able to correctly and completely detect all the buildings. The variable Sc_t formulation resulted in values of Sc_t that varied within the suggested values in ABL literature. The importance of this for ABL dispersion modeling cannot be underestimated.

Concerning the limitations of this study, a more comprehensive study would have included 12 wind di-

rections. Nevertheless, the only direction analyzed in this study is particularly meaningful, considering it is one of the most frequently occurring and one of the most concerning.
Besides, it should be emphasized that there is still room for improvement in the validation with the field data. Concerning the pollution measurements, only 1 high quality PM_{10} measurement device was available for the measurement campaign. In the future, measuring the concentration flowing into the zone of interest with the wind and the concentration in the zone of interest at the same time, will increase the reliability of the conclusions that can be drawn from the measurements. With respect to the wind velocity, the inflowing velocity magnitude was variable and too high during the measurement campaign. To overcome the problem of the variability of the inflowing wind in future research, it is suggested to model combinations of several wind directions and speeds and to measure for a longer period. This will result in validation data with sufficiently long periods where the conditions are very similar to inflow conditions used in the model.

In addition to the mentioned items in the study limitations, future work should focus on the employment of these and further remediation measures on other urban cases and on a sensitivity study of the applied measures: dimension, inclination and shape of the wind catchers, extent of the rooftop modification and number, orientation and location of the ESP devices. Also, the effect of atmospheric stability classes different from the neutral one on local pollution should be taken into account.

Acknowledgements

This work was supported by internal funding of the University of Antwerp and Université libre de Bruxelles.

References

Aarhus University, 2020. Description of the OSPM model. URL: https://envs.au.dk/en/research-areas/air-pollution-emissions-and-effects/the-monitoring-program/air-pollution-models/ospm/description-of-the-ospm-model/.

Abhijith, K.V., Gokhale, S., 2015. Passive control potentials of trees and on-street parked cars in reduction of air pollution exposure in urban street canyons. Environmental Pollution 204, 99–108. doi:10.1016/j.envpol.2015.04.013.

Abhijith, K.V., Kumar, P., Gallagher, J., McNabola, A., Baldauf, R., Pilla, F., Broderick, B., Di Sabatino, S., Pulvirenti, B., 2017. Air pollution abatement performances of green infrastructure in open road and built-up street canyon environments - A review. Atmospheric Environment 162, 71–86. doi:10.1016/j.atmosenv.2017.05.014.

Aliabadi, A.A., Krayenhoff, E.S., Nazarian, N., Chew, L.W., Armstrong, P.R., Afshari, A., Norford, L.K., 2017. Effects of Roof-Edge

Roughness on Air Temperature and Pollutant Concentration in Urban Canyons. Boundary-Layer Meteorology 164, 249–279. doi:10.1007/s10546-017-0246-1.

An, K., Wong, S.M., Fung, J.C.H., 2019. Exploration of sustainable building morphologies for effective passive pollutant dispersion within compact urban environments. Building and Environment 148, 508–523. doi:10.1016/j.buildenv.2018.11.030.

Apte, J.S., Messier, K.P., Gani, S., Brauer, M., Kirchstetter, T.W., Lunden, M.M., Marshall, J.D., Portier, J., Vermeulen, R.C.H., Hamburg, S.P., 2017. High-Resolution Air Pollution Mapping with Google Street View Cars: Exploiting Big Data. Environmental Science & Technology 51, 6999–7008. doi:10.1021/acs.est.7b00891.

Arkon, C.A., Özkol, U., 2014. Effect of urban geometry on pedestrian-level wind velocity. Architectural Science Review 57, 4–19. doi:10.1080/00038628.2013.835709.

Atkinson, R.W., Carey, I.M., Kent, A.J., van Staa, T.P., Anderson, H.R., Cook, D.G., 2013. Long-Term Exposure to Outdoor Air Pollution and Incidence of Cardiovascular Diseases. Epidemiology 24, 44–53. doi:10.1097/EDE.0b013e318276ccb8.

Ballari, M.M., Brouwers, H.J.H., 2013. Full scale demonstration of air-purifying pavement. Journal of Hazardous Materials 254, 406–414. doi:10.1016/j.jhazmat.2013.02.012.

Balogh, M., Parente, A., Benocci, C., 2012. Rans simulation of abl flow over complex terrains applying an enhanced k-ε model and wall function formulation: Implementation and comparison for fluent and openfoam. Journal of wind engineering and industrial aerodynamics 104, 360–368. doi:10.1016/j.jweia.2012.02.023.

Bazyar, J., Pourvakhshoori, N., Khankeh, H., Farrokhi, M., Delshad, V., Rajabi, E., 2019. A comprehensive evaluation of the association between ambient air pollution and adverse health outcomes of major organ systems: a systematic review with a worldwide approach. Environmental Science and Pollution Research 26, 12648–12661. doi:10.1007/s11356-019-04874-z.

Bechmann, A., 2006. Large-Eddy Simulation of Atmospheric Flow over Complex Terrain. Ph.D. thesis. Technical University of Denmark.

Beckerman, B., Jerrett, M., Brook, J.R., Verma, D.K., Arain, M.A., Finkelstein, M.M., 2008. Correlation of nitrogen dioxide with other traffic pollutants near a major expressway. Atmospheric Environment 42, 275–290. doi:10.1016/j.atmosenv.2007.09.042.

Blocken, B., Stathopoulos, T., Carmeliet, J., 2007. CFD simulation of the atmospheric boundary layer: wall function problems. Atmospheric Environment 41, 238–252. doi:10.1016/j.atmosenv.2006.08.019.

Blocken, B., Vervoort, R., van Hooff, T., 2016. Reduction of outdoor particulate matter concentrations by local removal in semi-enclosed parking garages: A preliminary case study for eindhoven city center. Journal of Wind Engineering and Industrial Aerodynamics 159, 80–98. doi:10.1016/j.jweia.2016.10.008.

Bonn, B., von Schneidemesser, E., Andrich, D., Quedenau, J., Gerwig, H., Lüdecke, A., Kura, J., Pietsch, A., Ehlers, C., Klemp, D., Kofahl, C., Nothard, R., Kerschbaumer, A., Junkermann, W., Grote, R., Pohl, T., Weber, K., Lode, B., Schönberger, P., Churkina, G., Butler, T.M., Lawrence, M.G., 2016. BAERLIN2014 – the influence of land surface types on and the horizontal heterogeneity of air pollutant levels in berlin. Atmospheric Chemistry and Physics 16, 7785–7811. doi:10.5194/acp-16-7785-2016.

Boonen, E., Beeldens, A., 2014. Recent Photocatalytic Applications for Air Purification in Belgium . Coatings 4, 553–573. doi:10.3390/coatings4030553.

Brost, R.A., Wyngaard, J.C., 1978. A model study of the stably stratified planetary boundary layer. Journal of the Atmospheric Sciences 35, 1427–1440. doi:10.1175/1520-0469(1978)035<1427:AMSOTS>2.0.CO;2.

Buccolieri, R., Salim, S.M., Leo, L.S., Di Sabatino, S., Chan, A., Ielpo, P., de Gennaro, G., Gromke, C., 2011. Analysis of local scale tree–atmosphere interaction on pollutant concentration in idealized street canyons and application to a real urban junction. Atmospheric Environment 45, 1702–1713. doi:10.1016/j.atmosenv.2010.12.058.

Buccolieri, R., Sandberg, M., Di Sabatino, S., 2010. City breathability and its link to pollutant concentration distribution within urban-like geometries. Atmospheric Environment 44, 1894–1903. doi:10.1016/j.atmosenv.2010.02.022.

Busini, V., Rota, R., 2014. Influence of the shape of mitigation barriers on heavy gas dispersion. Journal of Loss Prevention in the Process Industries 29, 13–21. doi:10.1016/j.jlp.2014.01.001.

Calvert, J.G., 1990. GLOSSARY OF ATMOSPHERIC CHEMISTRY TERMS - (RECOMMENDATIONS 1990). Pure and Applied Chemistry 62, 2167–2219. P. 2186.

Chew, L.W., Norford, L.K., 2019. Pedestrian-level wind speed enhancement with void decks in three-dimensional urban street canyons. Building and Environment 155, 399–407. doi:10.1016/j.buildenv.2019.03.058.

Chávez Yáñez, M., 2014. A Comprehensive Numerical Study of the Effects of Adjacent Buildings on Near-field Pollutant Dispersion. Ph.D. thesis.

Craft, T.J., Launder, B.E., Suga, K., 1996. Development and application of a cubic eddy-viscosity model of turbulence. International Journal of Heat and Fluid Flow 17, 108–115. doi:10.1016/0142-727X(95)00079-6.

Dabberdt, W.F., Hoydysh, W.G., 1991. Street canyon dispersion: sensitivity to block shape and entrainment. Atmospheric Environment 25, 1143–1153. doi:10.1016/0960-1686(91)90225-V.

Derudi, M., Bovolenta, D., Busini, V., Rota, R., 2014. Heavy gas dispersion in presence of large obstacles: selection of modeling tools. Industrial & Engineering Chemistry Research 53, 9303–9310. doi:10.1021/ie4034895.

Di Bernardino, A., Monti, P., Leuzzi, G., Querzoli, G., 2019. Turbulent schmidt number measurements over three- 3 dimensional cubic arrays. Boundary-Layer Meteorology 174, 231–250. doi:10.1007/s10546-019-00482-z.

Di Sabatino, S., Buccolieri, R., Pulvirenti, B., Britter, R., 2004. Simulations of pollutant dispersion within idealised urban-type geometries with cfd and integral models. Atmospheric environment 41, 8316–8329. doi:10.1016/j.atmosenv.2007.06.052.

Donzis, D.A., Aditya, K., Sreenivasan, K.R., Yeung, P.K., 2014. The turbulent schmidt number. Journal of Fluids Engineering 136. doi:10.1115/1.4026619.

EEA, 2018. Emissions of primary PM2.5 and PM10 particulate matter . URL: https://www.eea.europa.eu/data-and-maps/indicators/emissions-of-primary-particles-and-5/assessment-2. European Environment Agency. Accessed on 26 November 2019.

EEA, 2019a. Air pollutant emissions data viewer (Gothenburg Protocol, LRTAP Convention) 1990-2017 . URL: https://www.eea.europa.eu/data-and-maps/dashboards/air-pollutant-emissions-data-viewer-2. European Environment Agency. Accessed on 25 November 2019.

EEA, 2019b. Air quality in Europe - 2019 report. URL: https://www.eea.europa.eu/publications/air-quality-in-europe-2019/air-quality-in-europe-2019/viewfile#pdfjs.action=download. European Environment Agency.

EEA, 2019c. Air quality statistics. URL: https://www.eea.europa.eu/data-and-maps/dashboards/air-quality-statistics. European Environment Agcency. Accessed on 25 November 2019.

Ehrhard, J., Moussiopoulos, N., 2000. On a new nonlinear turbulence model for simulating flows around building-shaped structures. Journal of Wind Engineering and Industrial Aerodynamics 88, 91–99. doi:10.1016/S0167-6105(00)00026-X.

ENS Clean Air Solutions, 2018. Aufero. Innovative air purification system. URL: https://enstechnology.nl/wp-content/uploads/2018/03/ENS-Clean-Air-Leaflet-Aufero-2018-Q1.1-EN.pdf. Accessed on 21 July 2020.

EU, 2015. Directive 2008/50/EC of the European Parliament and of the Council of 21 May 2008 on ambient air quality and cleaner air for Europe. URL: https://eur-lex.europa.eu/eli/dir/2008/50/oj.

European Commission, 2004. Reclaiming city streets for people. Chaos or quality of life? URL: https://ec.europa.eu/environment/pubs/pdf/streets_people.pdf. accessed on 23 July 2020.

Franke, J., Hellsten, A., Schlünzen, H., Carissimo, B., 2007. Best practice guideline for the CFD simulation of flows in the urban environments. Technical Report. COST Action 732.

Fu, X., Liu, J., Ban-Weiss, G.A., Zhang, J., Huang, X., Ouyang, B., Popoola, O., Tao, S., 2017. Effects of canyon geometry on the distribution of traffic-related air pollution in a large urban area: Implications of a multi-canyon air pollution dispersion model. Atmospheric Environment 165, 111–121. doi:10.1016/j.atmosenv.2017.06.031.

Gallus, M., Akylas, V., Barmpas, F., Beeldens, A., Boonen, E., Boreave, A., Cazaunau, M., Chen, H., Daele, V., Doussin, J.F., Dupart, Y., Gaimoz, C., George, C., Grosselin, B., Herrmann, H., Ifang, S., Kurtenbach, R., Maille, M., Mellouki, A., Miet, K., Mothes, F., Moussiopoulos, N., Poulain, L., Rabe, R., Zapf, P., Kleffmann, J., 2015a. Photocatalytic de-pollution in the Leopold II tunnel in Brussels: NOx abatement results. Building and Environment 84, 125–133. doi:10.1016/j.buildenv.2014.10.032.

Gallus, M., Ciuraru, R., Mothes, F., Akylas, V., Barmpas, F., Beeldens, A., Bernard, F., Boonen, E., Boréave, A., Cazaunau, M., Charbonnel, N., Chen, H., Daële, V., Dupart, Y., Gaimoz, C., Grosselin, B., Herrmann, H., Ifang, S., Kurtenbach, R., Maille, M., Marjanovic, I., Michoud, V., Mellouki, A., Miet, K., Moussiopoulos, N., Poulain, L., Zapf, P., George, C., Doussin, J.F., Kleffmann, J., 2015b. Photocatalytic abatement results from a model street canyon. Environmental Science and Pollution Research 22, 18185–18196. doi:10.1007/s11356-015-4926-4.

Ghassoun, Y., Löwner, M.O., 2017. Land use regression models for total particle number concentrations using 2D, 3D and semantic parameters. Atmospheric Environment 166, 362–373. doi:10.1016/j.atmosenv.2017.07.042.

Gorlé, C., van Beeck, J., Rambaud, P., 2010. Dispersion in the wake of a rectangular building: validation of two reynolds-averaged navier–stokes modelling approaches. Boundary-layer meteorology 137, 115–133. doi:10.1007/s10546-010-9521-0.

Gousseau, P., Blocken, B., Stathopoulos, T., van Heijst, G.J.F., 2011. CFD simulation of near-field pollutant dispersion on a high-resolution grid: A case study by LES and RANS for a building group in downtown Montreal. Atmospheric Enivronment 45, 428–438. doi:10.1016/j.atmosenv.2010.09.065.

Gromke, C., Buccolieri, R., Di Sabatino, S., Ruck, B., 2008. Dispersion study in a street canyon with tree planting by means of wind tunnel and numerical investigations – Evaluation of CFD data with experimental data 42, 8640–8650. doi:10.1016/j.atmosenv.2008.08.019.

Gualtieri, C., Angeloudis, A., Bombardelli, F., Jha, S., Stoesser, T., 2017. On the values for the turbulent schmidt number in environmental flows 2. doi:10.3390/fluids2020017.

Guarnieri, M., Balmes, J.R., 2014. Outdoor air pollution and asthma. Lancet 383, 1581–1592. doi:10.1016/S0140-6736(14)60617-6.

Guerrini, G.L., Peccati, E., 2007. Photocatalytic cementitious roads for depollution, in: International RILEM Symposium on Photocatalysis, Environment and Construction Materials - TDP 2007, pp. 179–186.

Hang, J., Li, Y., 2010. Ventilation strategy and air change rates in idealized high-rise compact urban areas. Building and Environment 45, 2754–2767. doi:10.1016/j.buildenv.2010.06.004.

Hang, J., Li, Y., Sandberg, M., Buccolieri, R., Di Sabatino, S., 2012. The influence of building height variability on pollutant dispersion and pedestrian ventilation in idealized high-rise urban areas. Building and Environment 56, 346–360. doi:10.1016/j.buildenv.2012.03.023.

Hao, C., Xie, X., Huang, Y., Huang, Z., 2019. Study on influence of viaduct and noise barriers on the particulate matter dispersion in street canyons by CFD modeling. Atmospheric Pollution Research 10, 1723–1735. doi:10.1016/j.apr.2019.07.003.

Holmes, N., Morawska, L., 2006. A review of dispersion modelling and its application to the dispersion of particles: an overview of different dispersion models available. Atmospheric Environment 40, 6902–5928. doi:10.1016/j.atmosenv.2006.06.003.

Huang, H., Akutsu, Y., Arai, M., Tamura, M., 2000. A two-dimensional air quality model in an urban street canyon: evaluation and sensitivity analysis. Atmospheric Environment 34, 689–698. doi:10.1016/S1352-2310(99)00333-7.

Huang, Y.D., Hou, R.W., Liu, Z.Y., Song, Y., Cui, P.Y., Kim, C.N., 2019. Effects of Wind Direction on the Airflow and Pollutant Dispersion inside a Long Street Canyon. Aerosol and Air Quality Research 19, 1152–1171. doi:10.4209/aaqr.2018.09.0344.

Janhäll, S., 2015. Review on urban vegetation and particle air pollution - Deposition and dispersion. Atmospheric Environment 105, 130–137. doi:10.1016/j.atmosenv.2015.01.052.

Jeanjean, A.P.R., Gallagher, J., Monks, P.S., Leigh, R.J., 2017. Ranking current and prospective NO2 pollution mitigation strategies: An environmental and economic modelling investigation in oxford street, london. Environmental Pollution 225, 587–597. doi:10.1016/j.envpol.2017.03.027.

Juan, Y.H., Yang, A.S., Wen, C.Y., Lee, Y.T., Wang, P.C., 2017. Optimization procedures for enhancement of city breathability using arcade design in a realistic high-rise urban area. Building and Environment 121, 247–261. doi:10.1016/j.buildenv.2017.05.035.

Karagulian, F., Belis, C.A., Dora, C.F., Prüss-Ustün, A.M., Bonjour, S., Adair-Rohani, H., Amann, M., 2015. Contributions to cities' ambient particulate matter (pm): A systematic review of local source contributions at global level. Atmospheric environment 120, 475–483. doi:10.1016/j.atmosenv.2015.08.087.

Karlsruhe Institute of Technology, n.d. CODASC data base. URL: https://www.windforschung.de/CODASC.htm. (accessed on 10 August 2020).

Kastner-Klein, P., Plate, E., Fedorovich, E., 1997. Gaseous pollulant dispersion around urban-canopy elements: wind tunnel case studies. International Journal of Environment and Pollution 8, 727–737. 4th Workshop on Harmonization with Atmospheric Dispersion Modelling for Regulatory Purposes, 1996.

Keshavarzian, E., Jin, R., Dong, K., C.S. Kwok, K., Zhang, Y., Zhao, M., 2020. Effect of pollutant source location on air pollutant dispersion around a high-rise building. Applied Mathematical Modelling 81. doi:10.1016/j.apm.2020.01.019.

Kurppa, M., Hellsten, A., Auvinen, M., Raasch, S., Vesala, T., Jarvi, L., 2018. Ventilation and Air Quality in City Blocks Using Large-Eddy SimulationUrban Planning Perspective. Atmosphere 9. doi:10.3390/atmos9020065.

Li, F., Liu, J., Ren, J., Cao, X., 2018a. Predicting contaminant dispersion using modified turbulent schmidt numbers from different vortex structures. Building and Environment 130, 120–127. doi:10.1016/j.buildenv.2017.12.023.

Li, Z., Fung, J.C.H., Lau, A.K.H., 2018b. High spatiotemporal characterization of on-road PM2.5 concentrations in high-density urban areas using mobile monitoring. Building and Environment 143, 196–205. doi:10.1016/j.buildenv.2018.07.014.

Lien, F.S., Chen, W.L., Leschziner, M.A., 1996. Low reynolds-number eddy-viscosity modelling based on non-linear stress-strain/vorticity relations. Engineering Turbulence Modelling and Experiments 3 , 91–100.

Lin, Y., Chen, G., Chen, T., Luo, Z., Yuan, C., Gao, P., Hang, J., 2019. The influence of advertisement boards, street and source layouts on CO dispersion and building intake fraction in three-dimensional urban-like models. Building and Environment 150, 297–321. doi:10.1016/j.buildenv.2019.01.012.

Logan, J.A., 1983. Nitrogen oxides in the troposphere: Global and regional budgets. Journal of Geophysical Research 88, 10785–10807. doi:10.1029/JC088iC15p10785.

Longo, R., 2020. Advanced turbulence models for the simulation of air pollutants dispersion in urban area. Ph.D. thesis.

Longo, R., Bellemans, A., Derudi, M., Parente, A., 2020a. A multi-fidelity framework for the estimation of the turbulent schmidt number in the simulation of atmospheric dispersion. Building and Environment 185. doi:10.1016/j.buildenv.2020.107066.

Longo, R., Bellemans, A., Ferrarotti, M., Derudi, M., Parente, A., 2018. A new turbulent schmidt number formulation based on the local turbulence level, in: ETMM12 - 12th International ERCOFTAC Symposium on Engineering Turbulence Modelling and Measurements, Montpellier, France.

Longo, R., Ferrarotti, M., García Sánchez, C., Derudi, M., Parente, A., 2017. Advanced turbulence models and boundary conditions for flows around different configurations of ground-mounted buildings. Journal of wind engineering and industrial aerodynamics 167, 160–182. doi:10.1016/j.jweia.2017.04.015.

Longo, R., Ferrarotti, M., Parente, A., 2016. Cubic turbulence closures and dispersion models for flows around different configurations of ground-mounted buildings, in: ETMM11 - 11th International ERCOFTAC Symposium on Engineering Turbulence Modelling and Measurements, Palermo, Italy.

Longo, R., Fürst, M., Bellemans, A., Ferrarotti, M., Derudi, M., Parente, A., 2019. Cfd dispersion study based on a variable schmidt formulation for flows around different configurations of ground-mounted buildings. Building and Environment 154, 336–347. doi:10.1016/j.buildenv.2019.02.041.

Longo, R., Nicastro, P., Natalini, M., Schito, P., Mereu, R., Parente, A., 2020b. Impact of urban environment on savonius wind turbine performance: a numerical perspective. Renewable Energy 156, 407–422. doi:10.1016/j.renene.2020.03.101.

Löwner, M.O., Ghassoun, Y., 2018. THE INFLUENCE OF LEVELS OF DETAIL (LOD0-2) AND BUFFER SIZES ON PARAMETER EFFECTIVENESS FOR FINE DUST DISTRIBUTION MODELLING, in: 13TH 3D GEOINFO CONFERENCE 2018, pp. 41–48. doi:10.5194/isprs-annals-IV-4-W6-41-2018.

Maggos, T., Plassais, A., Bartzis, J.G., Vasilakos, C., Moussiopoulos, N., Bonafous, L., 2008. Photocatalytic degradation of NOx in a pilot street canyon configuration using TiO2-mortar panels. Environmental Monitoring and Assessment 136, 35–44. doi:10.1007/s10661-007-9722-2.

Mamaghani, A.H., Haghighat, F., Lee, C.S., 2017. Photocatalytic oxidation technology for indoor environment air purification: The state-of-the-art . Applied Catalysis B-Environmental 203, 247–269. doi:10.1016/j.apcatb.2016.10.037.

Manning, W.J., 2011. Urban environment: defining its nature and problems and developing strategies to overcome obstacles to sustainability and quality of life. Environmental Pollution 159, 1963–1964. doi:10.1016/j.envpol.2011.04.002.

Mei, D., Wen, M., Xu, X., Zhu, Y., Xing, F., 2018. The influence of wind speed on airflow and fine particle transport within different building layouts of an industrial city. Journal of the Air & Waste Management Association 68, 1038–1050. doi:10.1080/10962247.2018.1465487.

Merbitz, H., Detalle, F., Ketzler, G., Schneider, C., Lenartz, F., 2012. Small scale particulate matter measurements and dispersion modelling in the inner city of Liege, Belgium . International Journal of Environment and Pollution 50, 234–249. doi:10.1504/IJEP.2012.051196.

Merci, B., De Langhe, C., Lodefier, K., Dick, E., 2004. Axisymmetric impingement heat transfer with a nonlinear k-ϵ model. Journal of Thermophysics and Heat Transfer 18, 100–107. doi:10.2514/1.1378.

Meysman, F.J.R., De Craemer, S., 2018. CurieuzeNeuzen Vlaanderen: Het cijferrapport. Data retrieved from https://curieuzeneuzen.be/in-english/ (website with some English explanation, accessed on 4 November 2019).

Misawa, K., Sekine, Y., Kusukubo, Y., Sohara, K., 2020. Photocatalytic degradation of atmospheric fine particulate matter (PM2.5) collected on TiO(2)supporting quartz fibre filter. Environmental Technology 41, 1266–1274. doi:10.1080/09593330.2018.1530696.

Moonen, P., Defraeye, T., Dorer, V., Blocken, B., Carmeliet, J., 2012. Urban Physics: Effect of the micro-climate on comfort, health and energy demand. Frontiers of Architectural Research 1, 197–228. doi:10.1016/j.foar.2012.05.002.

Nguyen, V.H., Nguyen, B.S., Huang, C.W., Le, T.T., Nguyen, C.C., Le, T.T.N., Heo, D., Ly, Q.V., Trinh, Q.T., Shokouhimehr, M., Xia, C.L., Lam, S.S., Vo, D.V.N., Kim, S.Y., Le, Q.V., 2020. Photocatalytic NOx abatement: Recent advances and emerging trends in the development of photocatalysts. Journal of Cleaner Production 270. doi:10.1016/j.jclepro.2020.121912.

Niu, H., Wang, B., Liu, B., Liu, Y., Liu, J., Wang, Z., 2018. Numerical simulations of the effect of building configurations and wind direction on fine particulate matters dispersion in a street canyon. Environmental Fluid Mechanics 18, 829–847. doi:10.1007/s10652-017-9563-7.

OECD, 2012. Oecd environmental outlook to 2050: the consequences of inaction.

OECD, 2019. Air and GHG emissions. URL: https://data.oecd.org/air/air-and-ghg-emissions.htm#indicator-chart. doi:10.1787/93d10cf7-en. Accessed on 25 November 2019.

Oke, T.R., 1988. Street Design and Urban Canopy Layer Climate. Energy and Buildings 11, 103–113. doi:10.1016/0378-7788(88)90026-6.

Ollis, D.F., 2000. Photocatalytic purification and remediation of contaminated air and water, in: Comptes Rendus de l'Académie des Sciences - Series IIC - Chemistry. doi:10.1016/S1387-1609(00)01169-5.

OpenStreetMap, 2019. URL: https://www.openstreetmap.org/#map=16/51.2123/4.4340. Accessed on 8 November 2019. © OpenStreetMap contributors. Data of OpenStreetMap may be distributed, license description: https://www.openstreetmap.org/copyright.

Panagiotou, I., Neophytou, M.K.A., Hamlyn, D., Britter, R.E., 2013. City breathability as quantified by the exchange velocity and its spatial variation in real inhomogeneous urban geometries: An example from central London urban area. Science of the Total Environment 442, 466–477. doi:10.1016/j.scitotenv.2012.09.001.

Papailias, I., Giannakopoulou, T., Todorova, N., Demotikali, D., Vaimakis, T., Trapalis, C., 2015. Effect of processing temperature on structure and photocatalytic properties of g-C3N4. Applied Surface Science 358, 278–286. doi:10.1016/j.apsusc.2015.08.097.

Parente, A., Gorlé, C., van Beeck, J., Benocci., C., 2011a. A comprehensive modelling approach for the neutral atmospheric boundary layer: Consistent inflow conditions, wall function and turbulence model. Boundary-Layer Meteorology 140, 140–411. doi:10.1007/s10546-011-9621-5.

Parente, A., Gorlé, C., van Beeck, J., Benocci., C., 2011b. Improved k-epsilon model and wall function formulation for the rans simulation of abl flows. Journal of wind engineering and industrial aerodynamics 99, 267–278. doi:10.1016/j.jweia.2010.12.017.

Parente, A., Longo, R., Ferrarotti, M., 2017. CFD boundary conditions, turbulence models and dispersion study for flows around obstacles. VKI LS 2017-01. doi:10.35294/ls201701.parente.

Parente, A., Longo, R., Ferrarotti, M., 2019. Turbulence model formulation and dispersion modelling for the CFD simulation of flows around obstacles and on complex terrains. VKI LS 2019-03. doi:10.35294/ls201903.parente.

Peralta, C., Parente, A., Balogh, M., Benocci, C., 2014. Rans simulation of the atmospheric boundary layer over complex terrain with a consistent k-epsilon model formulation, in: 6th International Symposium on Computational Wind Engineering (CWE2014), Hamburg, Germany.

Piroozmand, P., Mussetti, G., Allegrini, J., Haji Mohammadi, M., Akrami, E., Carmeliet, J., 2020. Coupled CFD framework with mesoscale urban climate model: Application to microscale urban flows with weak synoptic forcing. Journal of Wind Engineering and Industrial Aerodynamics 197. doi:10.1016/j.jweia.2019.104059.

Pontiggia, M., Derudi, M., Alba, M., Scaioni, M., Rota, R., 2010. Hazardous gas releases in urban areas: Assessment of consequences through cfd modelling. Journal of Hazardous Materials 176, 589–596. doi:10.1016/j.jhazmat.2009.11.070.

Pospisil, J., Jicha, M., 2010. Particulate matter dispersion modelling along urban traffic paths. International Journal of Environment and Pollution 40, 26–35. doi:10.1504/IJEP.2010.030880.

Quarmby, S., Santos, G., Mathias, M., 2019. Air quality strategies and technologies: A rapid review of the international evidence.

Sustainability 11. doi:10.3390/su11102757.

Reynolds, A.J., 1975. The prediction of turbulent prandtl and schmidt numbers. International Journal of Heat and Mass Transfer 18, 1055–1069.

Ricciardelli, F., Polimeno, S., 2006. Some characteristics of the wind flow in the lower Urban Boundary Layer . Journal of Wind Engineering and Industrial Aerodynamics 94, 815–832. doi:10.1016/j.jweia.2006.06.003.

de Richter, R., Caillol, S., 2011. Fighting global warming: The potential of photocatalysis against CO2, CH4, N2O, CFCs, tropospheric O3, BC and other major contributors to climate change. Journal of Photochemistry and Photobiology C: Photochemistry Reviews 12, 1–19. doi:10.1016/j.jphotochemrev.2011.05.002.

Rijksoverheid, 2018. Emissiefactoren voor snelwegen en niet-snelwegen. URL: https://www.rijksoverheid.nl/documenten/publicaties/2018/03/15/emissiefactoren-voor-snelwegen-en-niet-snelwegen-2018. Accessed in 2018.

Roache, P., 1998. Verification and validation in computational science and engineering. Hermosa Publishers, Albuquerque, NM, USA.

Roache, P.J., 2009. Perspective: Validation—what does it mean? Journal of Fluids Engineering 131, 034503. doi:10.1115/1.3077134.

Salmond, J.A., Williams, D.E., Laing, G., Kingham, S., Dirks, K., Longley, I., Henshaw, G.S., 2013. The influence of vegetation on the horizontal and vertical distribution of pollutants in a street canyon . Science of The Total Environment 443, 287–298. doi:10.1016/j.scitotenv.2012.10.101.

Shalaby, H.M., Sherif, A., Altan, H., 2018. The impact of the informal area expansion on the urban natural ventilation of Alexandria. Innovative Infrastructure Solutions 3. doi:10.1007/s41062-017-0109-0.

Shayegan, Z., Lee, C.S., Haghighat, F., 2018. TiO2 photocatalyst for removal of volatile organic compounds in gas phase - A review. Chemical Engineering Journal 334, 2408–2439. doi:10.1016/j.cej.2017.09.153.

Shen, J., Gao, Z., Ding, W., Yu, Y., 2017. An investigation on the effect of street morphology to ambient air quality using six real-world cases. Atmospheric Environment 164, 85–101. doi:10.1016/j.atmosenv.2017.05.047.

Shen, Z., Wang, B., Cui, G., Zhang, Z., 2015. Flow pattern and pollutant dispersion over three dimensional building arrays. Atmospheric Environment 116, 202–215. doi:10.1016/j.atmosenv.2015.06.022.

Shi, Y., Xie, X., Fung, J.C.H., Ng, E., 2018. Identifying critical building morphological design factors of street-level air pollution dispersion in high-density built environment using mobile monitoring. Building and Environment 128, 248–259. doi:10.1016/j.buildenv.2017.11.043.

Tan, W., Li, C., Wang, K., Zhu, G., Liu, L., 2019. Geometric effect of buildings on the dispersion of carbon dioxide cloud in idealized urban street canyons. Process Safety and Environmental Protection 122, 271–280. doi:10.1016/j.psep.2018.12.020.

Tominaga, Y., 2012. Visualization of city breathability based on CFD technique: case study for urban blocks in Niigata City. Journal of Visualization 15, 269–276. doi:10.1007/s12650-012-0128-z.

Tominaga, Y., Mochida, A., Yoshie, R., Kataoka, H., Nozu, T., Yoshikawa, M., Shirasawa, T., 2008. Aij guidelines for practical applications of cfd to pedestrian wind environment around buildings. Journal of Wind Engineering and Industrial Aerodynamics 96, 1749–1761. doi:10.1016/j.jweia.2008.02.058.

Van Dingenen, R., Raes, F., Putaud, J.P., Baltensperger, U., Charron, A., Facchini, M.C., Decesari, S., Fuzzi, S., Gehrig, R., Hansson, H.C., Harrison, R.M., Huglin, C., Jones, A.M., Laj, P., Lorbeer, G., Maenhaut, W., Palmgren, F., Querol, X., Rodriguez, S., Schneider, J., ten Brink, H., Tunved, P., Torseth, K., Wehner, B., Weingartner, E., Wiedensohler, A., Wahlin, P., 2004. A european aerosol phenomenology-1: physical characteristics of particulate matter at kerbside, urban, rural and background sites in europe. Atmospheric Environment 38, 2561–2577. doi:10.1016/j.atmosenv.2004.01.040.

Vardoulakis, S., Kettle, R., Cosford, P., Lincoln, P., Holgate, S., Grigg, J., Kelly, F., Pencheon, D., 2018. Local action on outdoor air pollution to improve public health. International Journal of Public Health 63, 557–565. doi:10.1007/s00038-018-1104-8.

Vervoort, R., Blocken, B., van Hooff, T., 2019. Reduction of particulate matter concentrations by local removal in a building courtyard: Case study for the delhi american embassy school. Science of The Total Environment 686, 657–680. doi:10.1016/j.scitotenv.2019.05.154.

Vlaamse overheid, 2019. Geopunt-kaart. URL: http://www.geopunt.be/. Accessed on 20 December 2019.

VMM, 2018. ANNUAL AIR REPORT – FLANDERS (BELGIUM). Emissions 2000-2016 and air quality in Flanders in 2017. Flanders Environment Agency.

VMM, 2019. Luchtkwaliteit in de antwerpse agglomeratie - jaarrapport 2018.

Voordeckers, D., Lauriks, T., Denys, S., Billen, P., Tytgat, T., Van Acker, M., in press. Guidelines for passive control of traffic-related air pollution in street canyons: an overview for urban planning. Landscape and Urban Planning .

Vos, P.E.J., Maiheu, B., Vankerkom, J., Janssen, S., 2013. Improving local air quality in cities: To tree or not to tree? Environmental Pollution 183, 113–122. doi:10.1016/j.envpol.2012.10.021.

Wadlow, I., Paton-Walsh, C., Forehead, H., Perez, P., Amirghasemi, M., Guérette, É.A., Gendek, O., Kumar, P., 2019. Understanding spatial variability of air quality in sydney: Part 2—a roadside case study. Atmosphere 10, 217. doi:10.3390/atmos10040217.

van Walsem, J., Roegiers, J., Modde, B., Lenaerts, S., Denys, S., 2018. Integration of a photocatalytic multi-tube reactor for indoor air purification in HVAC systems: a feasibility study. Environmental Science and Pollution Research 25, 18015–18026. doi:10.1007/s11356-018-2017-z.

van Walsem, J., Roegiers, J., Modde, B., Lenaerts, S., Denys, S., 2019. Proof of concept of an upscaled photocatalytic multi-tube reactor: A combined modelling and experimental study. Chemical Engineering Journal 378, 18015–18026. doi:10.1016/j.cej.2019.122038.

Wang, Z., Xie, X., Wang, X., Mahmood, A., Qiu, H., Sun, J., 2019. Difference of photodegradation characteristics between single and mixed VOC pollutants under simulated sunlight irradiation. Journal of Photochemistry and Photobiology A: Chemistry 384, 112029. doi:10.1016/j.jphotochem.2019.112029.

Wedding, J.B., Lombardi, D.J., Cermak, J.E., 1977. A Wind Tunnel Study of Gaseous Pollutants in City Street Canyons. Journal of the Air Pollution Control Association 27, 557–566. doi:10.1080/00022470.1977.10470456.

White, A.J., Bradshaw, P.T., Hamra, G.B., 2018. Air Pollution and Breast Cancer: a Review. Current Epidemiology Reports 5, 92–100. doi:10.1007/s40471-018-0143-2.

WHO, 2018. WHO ambient (outdoor) air quality database Summary results, update 2018. URL: https://www.who.int/airpollution/data/AAP_database_summary_results_2018_final2.pdf?ua=1.

WHO, 2019. Ambient air pollution: Pollutants. URL: https://www.who.int/airpollution/ambient/pollutants/en/. Accessed on 26 November 2019.

Xie, X.m., Wang, J.s., Huang, Z., 2009. Traffic Emission Transportation In Street Canyons. Journal of Hydrodynamics 21, 108–117. doi:10.1016/s1001-6058(08)60125-0.

Xie, Z.T., Castro, I.P., 2009. Large-eddy simulation for flow and dispersion in urban streets. Atmospheric Environment 43, 2174–2185. doi:10.1016/j.atmosenv.2009.01.016.

Yassin, M.F., 2013. Numerical modeling on air quality in an urban environment with changes of the aspect ratio and wind direction. Environmental Science and Pollution Research 20, 3975–3988. doi:10.1007/s11356-012-1270-9.

Yu, H., Thé, J., 2016. Validation and optimization of SST k-$/omega$ turbulence model for pollutant dispersion within a building array.

Atmospheric Environment 145, 225–238. doi:10.1016/j.atmosenv.2016.09.043.

Zhang, G.X., Liu, Y.Y., Hashisho, Z., Sun, Z.M., Zheng, S.L., Zhong, L.X., 2020. Adsorption and photocatalytic degradation performances of TiO2/diatomite composite for volatile organic compounds: Effects of key parameters. Applied Surface Science 525. doi:10.1016/j.apsusc.2020.146633.

Zhang, H., Xu, T., Wang, Y., Zong, Y., Li, S., Tang, H., 2016. Study on the influence of meteorological conditions and the street side buildings on the pollutant dispersion in the street canyon. Building Simulation 9, 717–727. doi:10.1007/s12273-016-0304-5.

Zhang, K., Chen, G., Wang, X., Liu, S., Mak, C.M., Fan, Y., Hang, J., 2019. Numerical evaluations of urban design technique to reduce vehicular personal intake fraction in deep street canyons. Science of the Total Environment 653, 968–994. doi:10.1016/j.scitotenv.2018.10.333.

Zhong, J., Cai, X.M., Bloss, W.J., 2016. Coupling dynamics and chemistry in the air pollution modelling of street canyons: a review. Environmental Pollution 214, 690–704. doi:10.1016/j.envpol.2016.04.052.